Bulletin of Earthquake Engineering
https://doi.org/10.1007/s10518-025-02178-x

REVIEW ARTICLE

# Fragility curves of URM buildings in aggregate considering the interaction with soil and among nearby footings

**E. Zeolla[1] · A. Brunelli[2] · F. de Silva[3] · S. Cattari[2] · S. Sica[1]**

Received: 1 October 2024 / Accepted: 13 April 2025


**Abstract**
The paper examines unreinforced masonry (URM) buildings, which are common in small historic centres around the world. These buildings are often constructed in aggregate, a configuration that not only results in significant structural interaction but also interaction with and through the foundation soil. The seismic performance of an aggregate can be influenced by foundation-soil-foundation interaction (FSFI), in addition to standard soil-foundation-structure interaction (SFSI) and site effects (SE). While reliable and time-efficient approaches are available in the literature to address all these issues for standalone buildings, buildings in aggregate are frequently modelled as isolated and fixed at their base, particularly when developing fragility curves. This paper investigates the effects of SFSI and FSFI on the period and damping ratio estimates of typical URM buildings. Specifically, it examines the impact of SE, SFSI, and FSFI on the fragility curves of two aggregated URM buildings. These latter are representative of Visso, a town heavily affected by the 2016–2017 Central Italy earthquake, known for site amplification phenomena due to soft soils. Fragility curves were developed through nonlinear dynamic analyses of equivalent 3D frame models of the two archetypes, analysed under both fixed and compliant base conditions. In the latter scenario, the structural model is equipped with springs at its base, with stiffness first calibrated to account for SFSI effects and subsequently adjusted to include the additional FSFI contribution. The results indicate a higher fragility in the fixed-base model. Specifically, the ratio of the median values of the fragility curves for the compliant base model to the fixed-base model ranges from 20 to 60%. Finally, the results from the cross-interacting models exhibited slightly higher values than those considering only SFSI, suggesting a moderate impact from the additional contribution of footing-footing interaction, at least for the case studies examined.

**Keywords** Impedance function · Soil-structure interaction · Soil-foundation-structure interaction · Fragility curves · Masonry structures · Nonlinear dynamic analyses

Extended author information available on the last page of the article

Published online: 26 May 2025

## 1 Introduction

This paper examines unreinforced masonry (URM) buildings in aggregate, which are often modelled as isolated and fixed at the base, particularly when developing fragility curves. The aim is to address this gap by investigating the effects of foundation-soil-foundation interaction (FSFI) and standard soil-foundation-structure interaction (SFSI) on the period and damping ratio estimates of typical URM buildings.

The fragility curves are commonly used to estimate the potential damage caused by earthquakes. Among the different approaches available in the literature for deriving fragility curves (Rossetto et al. 2014; Chieffo and Formisano 2019; Cattari et al. 2024) -namely empirical, mechanical-analytical, and mechanical-numerical- this paper refers to the latter, which is particularly well-suited to addressing the main objectives of the present study. Firstly, as already mentioned, these curves are often derived by neglecting important factors such as site, and SFSI effects. However, some studies have considered these additional sources of hazard and vulnerability for masonry buildings (e.g., Formisano et al. 2021; Brunelli et al. 2021a, 2021b, 2022a, b, c; Piro et al. 2020; de Silva et al. 2018; De Angelis et al. 2022a, b; Ambrosino and Sica 2024) or even reinforced concrete structures (Ademović et al. 2022; Sextos et al. 2018; Ambrosino et al. 2023), revealing that site amplification effects, without soil interaction, increase the estimated damage.

This information is particularly important when assessing building safety in European historic centers, often located in alluvial valleys (Garini et al. 2020; Brunelli et al. 2022a, b, c) or on hilltop for defensive purposes and may consequently be affected by significant stratigraphic and topographic site effects.

Historic centres typically consist of buildings founded on shallow foundations that are only marginally embedded in the overlying soil, which often possess poor mechanical properties. These buildings, constructed over centuries, now form aggregates with interacting elements. This interaction extends to the masonry wall foundations through the underlying soil. In general, smaller urban centres are characterized by structures that reflect a traditional, rustic architectural style, built from local materials such as stone, brick, and wood. These buildings are generally simple in design, featuring thick walls and small rooms, and are often constructed in close proximity, contributing to a cohesive urban fabric. While the spacing between load-bearing walls and the sizes of rooms can vary considerably from one building to another, in minor historic centres, the spacing is typically narrow. This compact arrangement was often used to maximize space within the city walls.

The buildings constructed in aggregate, with interacting parts and a variety of materials and construction techniques, are quite common (Carocci 2012). This results in varying states of preservation, which increases their vulnerability. Even within older buildings, room sizes can differ widely depending on internal layouts and alterations made over time. In contrast, major historic centres, such as those in Rome, Florence, Venice, or Naples, are characterized by greater extent and complexity. These centres contain a diverse array of structures of national and international significance, reflecting the historical and cultural richness of the cities. Such buildings often exhibit monumental and magnificent architecture, influenced by Renaissance, Baroque, Neoclassical, and other styles. Government palaces or aristocratic residences are frequently distinguished by larger and taller halls, often topped with vaults. Examples of some of the most common structural types with varying geometric features are shown in Fig. 1.

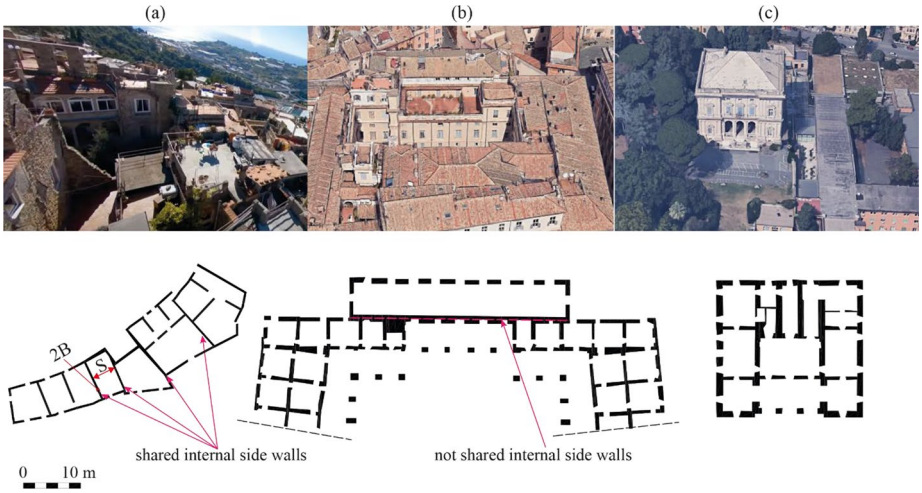


**Fig. 1** Examples of recurring building families in historic centers: (**a**) poor, small dwellings and URM aggregates, (**b**) medium sized houses and large buildings, (**c**) palaces of nobility

From the seismic vulnerability assessment perspective, buildings in aggregate pose additional numerical concerns compared to isolated structures, especially how simulating the possible pounding effects.

Although various studies have attempted to address this issue (Ulrich et al. 2015; Formisano 2017; Chiumiento and Formisano 2019; Battaglia et al. 2021; Valluzzi et al. 2022; Malomo and Dejong 2022; Bianchini et al. 2023; Zhang et al. 2024; Pinasco et al. 2024), the impact of boundary conditions imposed by neighbouring structural units (SUs) on the analysis of the single SU, as if it were isolated, remains a subject of ongoing debate in the literature (Demsic et al. 2024; Ponte et al. 2024; Salvatori et al. (2024; Villar et al. 2024). Moreover, in addition to site conditions, another aspect to consider when evaluating the seismic behaviour of these buildings is the proximity between the building foundations. Since the involved distances are often very small or absent, multiple interactions are likely to arise between their foundations (FSFI) and therefore cross interaction phenomena may constitute a relevant problem.

Site amplification can be quantified quite efficiently using linear equivalent analyses (Régnier et al. 2018), which are effective for the range of shear strains typically mobilized by common earthquakes and, in some cases, by rare events. However, this approach does not address situations where the soil reaches a failure state (e.g., liquefaction or slope instability), which require completely different analytical methods. Moreover, the intensity measures and engineering demand parameters commonly used in seismic fragility curves may not fully capture the complexity of these extreme conditions.

The coupled approaches used to simulate SFSI (Azadi and Soltani 2010; Güllü and Jaf 2016; Fathi et al. 2020; Outayeb et al. 2023) and eventually FSFI effects (Tsogka and Wirgin 2003; Padron et al. 2008, 2009; Bybordiani and Arici 2019; Bordón et al. 2019), are challenging to apply in the construction of fragility curves due to the large number of structural analyses required.

Conversely, uncoupled approaches present a valid alternative. In these methods, the base of the structural model is equipped with springs and dashpots, with stiffness and damping parameters derived from soil-foundation impedance functions proposed in the literature (Mylonakis et al. 2006 or Pais and Kausel 1988) and also suggested in NIST (2012). This model is reliable if the calibration of the impedance functions accounts for the nonlinear effects mobilized by each input motion. This calibration can be performed using a linear equivalent approach (see Brunelli et al. 2022a), similar to site response analyses.

The study of dynamic interaction between foundations of the same structure or between adjacent structures is complex and influenced by numerous factors, including building layout, dynamic properties of structures, ground conditions and seismic excitation, among others. Developing a standardized method that incorporate all these factors in a single model is challenging. A recent study by Zeolla et al. (2023, 2024) proposed adapting the well-established substructure approach to solve cross-interaction problems involving multiple identical shallow foundations. In the research vein of previous works (Mulliken and Karabalis 1998; Qian and Beskos 1995, 1996; Betti 1997), impedance functions were computed through 3D numerical analyses using a suite of finite difference models representing two or three shallow foundations positioned at varying distances. Zeolla et al. (2023 and 2024) proposed groups of coefficients that modify the impedance functions of a single foundation to account for FSFI effects, depending on the foundation-to-foundation spacing.

Despite the abovementioned modelling strategies and developments in FSFI formulations, fragility curves that account for SE, SFSI are limited, and there are currently no examples that consider the effects of FSFI.

The objective of this study is to address this gap starting from a well-documented case study: the historic center of Visso, which experienced severe damage during the 2016–2017 earthquake sequence and notable site effects. Most of the buildings in Visso are URM building in aggregate, and the alluvial soil deposit strongly influenced the suffered damage scenario (Formisano et al. 2021; Brunelli et al. 2021a, 2022a, b, c). The fragility curves were developed using two selected archetypes representative of URM buildings in aggregate and explicitly considering typical failure mechanisms such as in-plane response, local mechanisms, and pounding effects. This paper compares results obtained with and without cross-interaction (FSFI) in terms of impedance values, periods of the coupled soil-structure system, equivalent damping, and simulated damage based on real earthquake recordings. Finally, the modified impedances were used to evaluate the effects of cross-interaction on the fragility curves.

## 2 Analytical approach to estimate FSF interaction on shallow foundations

As anticipated in the introduction, Zeolla et al. (2023, 2024) proposed closed-form equations for group coefficients for each degree of freedom of the foundation. These group factors enable the modification of the static and dynamic stiffness of an individual foundation to account for the presence of neighboring foundations. This approach allows the target foundation to be modeled as "isolated," but with adjusted stiffnesses that incorporate the effects of FSFI. In particular, the static stiffness of each foundation in a group ($K_{SFSI,\ i}$)

is derived from the static stiffness of a single foundation ($K_{single,\ i}$) through the following expression:

$$K_{SFSI,i} = (1 - \alpha_i) K_{single,i} \tag{1}$$

where $i$ denotes the degree of freedom of the foundation being considered and $\alpha_i$ is given as a function of the ratio between the foundation-foundation distance ($S$) and the half-width of the foundation ($B$) using the exponential law:

$$\alpha_i = a_i \exp[b_i (S/B)] \tag{2}$$

with:

$$a_i = c_{1a} \exp(d_{1a}(H/B)) + c_{2a} \exp(d_{2a}(H/B)) + c_{3a} \tag{3}$$

$$b_i = c_{1b} \exp(d_{1b}(H/B)) + c_{2b} \exp(d_{2b}(H/B)) + c_{3b} \tag{4}$$

where $H$ is the thickness of the deformable soil layer. If $H/B$ goes to infinity, the formulas provide solutions for the half-space. Note that Eq. (2) is a negative exponential law ($b_i$ <1), hence $\alpha_i$ decreases with $S/B$.

The coefficients $c_{1a}$, $c_{2a}$, $c_{3a}$, $d_{1a}$, $d_{2a}$, $c_{1b}$, $c_{2b}$, $c_{3b}$, $d_{1b}$, $d_{2b}$ are defined in Zeolla et al. 2024 for a footing in couple, as well as for a lateral and a central footing of a triplet. The coefficients are not provided for a group of four footings or larger because the interaction among the first and the fourth foundations resulted negligible, considering the typical span length of buildings. In the analyses conducted by Zeolla et al. (2023, 2024), dynamic damping characteristics were found to be slightly affected by the interaction between foundations, therefore no correction factors were derived.

In conclusion, in the present case, the interaction between the foundations was only taken into account in the static part of the impedance.

### 2.1 Influence of building class on cross interaction

This section examines masonry buildings used for residential purposes, categorized into three main classes based on plan and elevation dimensions. Specifically, archetypes representing these three classes, as illustrated in Fig. 1, are considered.

Class 1 comprises low-rise dwellings (1–2 storeys), typical of small historic centres, usually characterized by an architectural configuration with a few small rooms. In general, these structural units are situated close to one another, forming aggregate configurations. In such cases, adjacent structural units (SUs) may or may not share internal side walls. If two SUs are independent in bearing vertical loads, it is expected that each has its own foundation, resulting in two adjacent walls with separate foundations. Otherwise, SUs typically share an internal side wall (see Fig. 1a).

Class 2 includes medium-rise buildings with larger dimensions and architectural configurations featuring more rooms, typical of larger urban settlements. Class 3 consists of palaces, which are usually characterized by slender walls, greater interstorey heights, and larger rooms.

For the three identified building classes, the reduction in the static stiffness of the foundation due to the proximity of foundations within the same building was estimated. Additionally, given that the urban layout of old town centres often features narrow streets with small distances between buildings (1–3 m or even less), this proximity between foundations was also considered, particularly for Classes 2 and 3.

Depending on the class of the buildings, foundation sizes (*2B, 2L*) and the plausible range of distances between the foundations of the walls of the same building (*S*) or that of adjacent buildings ($S_b$) were assumed, as listed in Table 1 as shown in Fig. 1. These ranges were defined on basis of some typical in-plan and elevation configurations of the Italian building stock, which the Authors have examined in various research projects along the years.

First, the formulas proposed by Gazetas (1991) were applied to calculate the impedance function of a single footing situated on the surface of a half-space with a shear wave velocity $V_S$ = 100 m/s, a shear modulus G = 19 MPa and a Poisson coefficient ν = 0.3. The adopted $V_S$ value is consistent with that characterizing the soil volume affected by the foundation motion in the subsoil profiles described in Sect. 3.1 (see Fig. 6). The resulting values were then adjusted using Eq. (1) to account for FSFI. Table 2 lists the coefficients $a_i$ and $b_i$ employed in Eq. (1) for each degree of freedom, whether for the central or lateral foundation of the same building or for two foundations of nearby buildings. For a graphical representation, reference could be made to Fig. 2. Note that $a_i$ and $b_i$ coincide with $c_{3a}$ and $c_{3b}$ for the half-space.

Once the *S/B* ratios were established, the modified stiffnesses were computed using the corrective $\alpha_i$- coefficients. Figure 2 shows the ratio between the stiffness of the foundation in group and that of a single foundation, $\frac{K_{FSFI,i}}{K_{single,i}}$, as a function of *S/B*. Figure 2a refers to an inner foundation, flanked by other foundations on both the right and left at equal distances. Figure 2b considers a lateral footing influenced by the presence of the two adjacent foundations immediately beside it. The coefficients $a_i$ and $b_i$ adopted are listed in the first and second column of Table 2.

For the case of just two nearby foundations, Fig. 2c shows the same functions obtained using the regression coefficients in the third section (labelled as "nearby") of Table 2. These last coefficients may also turn useful when a foundation is positioned at a different distance between two adjacent footings, such as in irregular building layouts. In Fig. 2d, the change in stiffness caused by the presence of an edge foundation belonging to a neighbouring building is evaluated; smaller $S_b/B$ ratios refer to the cases representative of adjacent foundations of two SUs of a URM aggregate of buildings, by assuming $a_i$ and $b_i$ coefficients consistent with the third column of Table 2.

As observed in Fig. 2, the translational motions (xx, yy and zz) are most affected by cross-interaction with the greatest impact occurring in the horizontal Y-axis, which aligns with the direction of footing proximity. This pronounced effect is due to the significant interference of the pressure bulbs associated with translational motion along the Y-axis.

As expected, the stiffness reduction due to cross interaction is most pronounced for the central footing (Fig. 2a), which is influenced by the motion of both equally-spaced adjacent footings. The rocking stiffness (around both the X and Y axes) decreases rapidly, with the interaction effect becoming negligible for *S/B* values greater than 4. Notably, for rocking around the X-axis, the ratio is slightly greater than one, indicating an increase in stiffness

**Table 1** Geometric features considered for the computation of the static stiffness for the examined URM archetypes

| Class | Description | 2B [m] | 2 L [m] | S (distance between foundation of the same building i.e. distance between parallel walls) [m] | $S_b$ (distance between foundation of neighbouring buildings) [m] |
|---|---|---|---|---|---|
| 1 | small SUs, typical of URM buildings in. aggregate | 0.6–1 | 6–15 | 2–6 | 0.5 -2 |
| 2 | Medium- size houses | 1–1.5 | 6–16.5 | 9–13 | 0.5 -2 |
| 3 | large buildings, palaces | 1.5–2 | 8–20 | 11–17 | 0.5 -2 |

when the foundations are grouped. This is attributed to the constraining effect the foundations exert on each other during rotation, as no detachment is allowed.

When examining the interaction between the foundations of the same building (Fig. 2a-c), the Class 1 buildings experience a more significant reduction in stiffness. This is due to smaller *S/B* ratios, which results in higher $\alpha_i$ coefficients regulating the cross interaction between the nearby foundations. In contrast, Classes 2 and 3, characterized by larger S/B ratios, exhibit a smaller reduction in stiffness, approximately 10%, except for rocking stiffnesses.

When the interaction between neighbouring buildings is considered (Fig. 2d), the $S_b$/B ratios are notably lower ($0.5B < S_b < 2B$) than those pertaining to the foundations within the same building. This occurs because although the same $S_b$ values are assumed (as shown in the last column of Table 1), the half-width *B* of the foundations increases moving from Class 1 to Class 3. As a result, the variability range for Class 3 is shifted to the left. The change in rocking stiffnesses is also no longer negligible over the range of $S_b$/B ratios considered, particularly for Class 3, and to a lesser extent for Class 2 and 1 For instance, under these conditions, the increase in $K_{rx,FSFI}$ can vary between 10 and 20% for Class 3 and for the smaller $S_b$/B ratios of Classes 1 and 2 Conversely, a decrease is observed for all other degrees of freedom. This suggests that, while Classes 2 and 3 are only mildly affected by cross-interaction between their own foundations, they are not immune to cross interaction in a broader sense, as they can still interact with the foundations of the surrounding buildings.

### 2.2 Evaluation of period and damping ratio through the replacement oscillator approach

The impact of SFSI and FSFI was also evaluated on the dynamic properties of the building classes considered in Sect. 2.1. To this aim, the variation of the period ($T^*$) and the damping ratio ($\beta^*$) with respect to the fixed base condition ($T_0$ and $\beta_0$) was evaluated using the analytical formulas based on the "replacement oscillator" approach (Maravas et al. 2014). As well known, the replacement oscillator is a simplified single-degree-of-freedom (SDOF) model used to approximate the dynamic behavior of a more complex soil-structure system. The equivalent oscillator has the same dynamic properties (i.e., natural period and damping ratio) as the original system with contribution of soil-structure interaction, while maintaining the same mass and geometric features of the structure. For such an aim, the base of the equivalent SDOF needs to be equipped with springs and dashpots to simulate the soil-foundation impedance (Gazetas 1991; Maravas et al. 2014). The replacement oscillator is generally used for a first approximated estimation of the effect of soil-foundation-structure interaction (SFSI). In this vein, it was adopted to investigate the impact of SFSI on the typical URM isolated building, accounting for the cross interaction among the foundations of the same building, and the effect of an adjacent building, that is the case of an aggregate.

To save time, in this work, the calculations were executed through the web-app "0D-In" developed by de Silva and Silvestri (2025) and available at https://dynatools.it/odin. This tool facilitates sensitivity analyses on the impact of SFSI using the following dimensionless parameters: the structural slenderness ratios, *h/B*; the foundation aspect ratio, *L/B*; the structure-to-soil relative mass, $\delta = \frac{m}{(\rho_s \pi B^2 h)}$; and the soil-to-structure relative stiffness, $\sigma = \frac{V_s T_0}{h}$. The ranges for these dimensionless parameters were established based on the typical minimum and maximum values of the structural height, h, mass, m, and the fixed-

**Table 2** Exponential law coefficient a.i. and bi for Eq. 3a and 3b respectively

| Central | | | | Lateral | | | | Nearby | | | |
|---|---|---|---|---|---|---|---|---|---|---|---|
| $\mathbf{a_{zz}}$ | 0.56 | $\mathbf{b_{zz}}$ | -0.15 | $\mathbf{a_{zz}}$ | 0.35 | $\mathbf{b_{zz}}$ | -0.15 | $\mathbf{a_{zz}}$ | 0.28 | $\mathbf{b_{zz}}$ | -0.18 |
| $\mathbf{a_{yy}}$ | 0.58 | $\mathbf{b_{yy}}$ | -0.09 | $\mathbf{a_{yy}}$ | 0.39 | $\mathbf{b_{yy}}$ | -0.09 | $\mathbf{a_{yy}}$ | | $\mathbf{b_{yy}}$ | -0.10 |
| $\mathbf{a_{xx}}$ | 0.54 | $\mathbf{b_{xx}}$ | -0.16 | $\mathbf{a_{xx}}$ | 0.35 | $\mathbf{b_{xx}}$ | -0.15 | $\mathbf{a_{xx}}$ | | $\mathbf{b_{xx}}$ | -0.17 |
| $\mathbf{a_{rx}}$ | -0.88 | $\mathbf{b_{rx}}$ | -1.01 | $\mathbf{a_{rx}}$ | -0.30 | $\mathbf{b_{rx}}$ | -0.72 | $\mathbf{a_{ry}}$ | | $\mathbf{b_{rx}}$ | -0.66 |
| $\mathbf{a_{ry}}$ | 0.43 | $\mathbf{b_{ry}}$ | -0.42 | $\mathbf{a_{ry}}$ | 0.24 | $\mathbf{b_{ry}}$ | -0.44 | $\mathbf{a_{rx}}$ | -0.29 | $\mathbf{b_{ry}}$ | -0.51 |

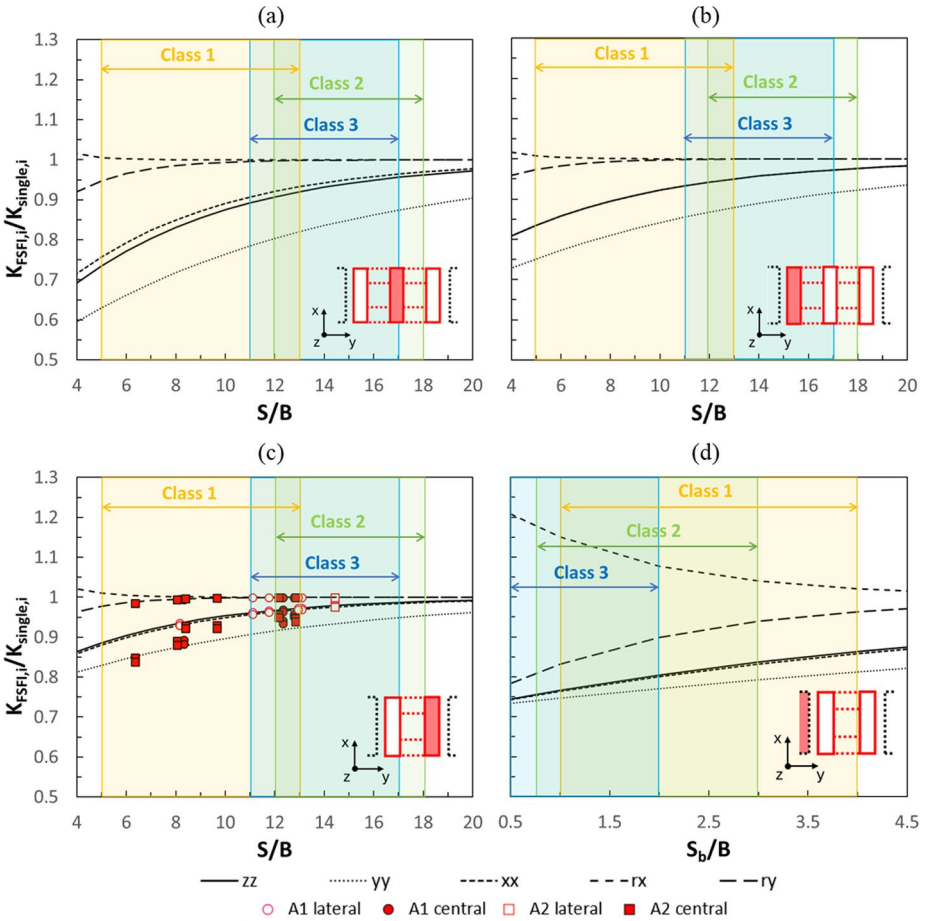


**Fig. 2** Stiffness ratios $K_{FSFI,\ i}/K_{single,\ i}$ versus S/B for the three building classes considered. Each curve refers to a different degree of freedom of the foundation (zz, yy, xx, rx and ry). The schemes superimposed to the charts indicate the position of the foundation within the group: (**a**) central and (**b**) lateral in the case of a group of three foundations or (**c**) two foundations and (**d**) next to a foundation belonging to a neighbouring building. The red indicators refer to the values of $K_{FSFI,\ i}/K_{single,\ i}$ obtained for the lateral and central foundations (empty and full indicators respectively) of the two aggregates which are the subject of the case study (aggregates A1 and A2 represented by circles and squares respectively) described further in Sect. 3

**Table 3** Minimum and maximum values of the dynamic properties considered for the three structural classes

| Properties | Class 1 min-max | Class 2 min-max | Class 3 min-max |
|---|---|---|---|
| Mass "*m*" [Mg] | 470–3100 | 1000–3600 | 1700–4500 |
| Height "*h*" [m] | 2.8–12 | 2.8–14.8 | 5.2–18 |
| Fix base period "$T_0$" [s] | 0.1–0.31 | 0.1–0.46 | 0.2–0.62 |
| Structural slenderness ratio "*h/B*" | 5.6–40 | 3.7–29 | 5.2–24 |
| Foundation aspect ratio "*L/B*" | 6–15 | 4–11 | 4–10 |
| Dimensionless distance between foundations (same building) "*S/B*" | 5–13 | 12–18 | 11–17 |
| Dimensionless distance between foundations (neighbouring building) "$S_b/B$" | 1–3 | 0.7–3 | 0.5–2 |
| Structure-to-soil relative mass "$\delta$" | 112.5–480.9 | 106.4–163 | 54.8–74.5 |

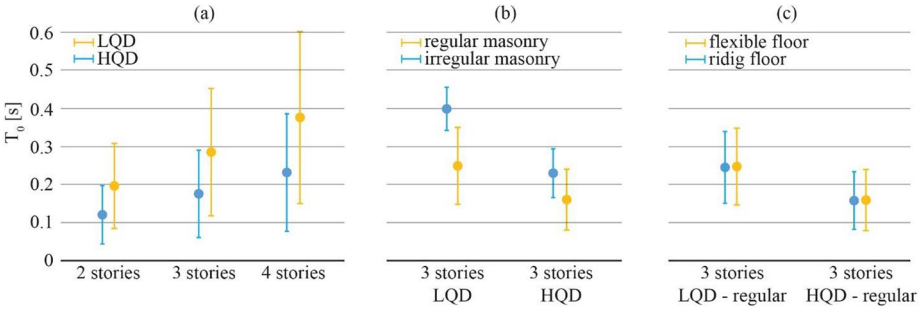


**Fig. 3** Variation of periods for fixed-base structures characterized by (**a**) LQ and HQ details; (**b**) regular and irregular masonry type and (**c**) flexible and rigid diaphragm type for regular masonry type

base fundamental period, $T_0$, as specified in Table 3 for each building class. In detail, the slenderness ratio is minimized by the maximum values of B (deduced from Table 1) and maximized by the smallest one. The same applies to the other dimensionless parameters. In this calculation, the soil hysteretic damping ratio and the structural damping ratio were kept constant at 1% and 3%, respectively, while the ratio L/B was varied according to the values reported in Table 3. The values of *B* are deduced from Table 1 for the three building classes.

Figure 3a shows the variation in period for two-, three- and four-story buildings characterized by different structural details as typical of existing URM buildings, i.e. with (High Quality Details - HQD) and without (Low Quality Details - LQD) tensile resistant elements placed at floor level, such as tie-rods or RC-curbs; in general, lower periods (i.e., stiffer structures) are associated to the presence of HQD. The reference values for the dynamic properties of such systems have been computed through the DBV-Masonry mechanical-analytical model (Lagomarsino et al. 2014; Cattari et al. 2021) using the same proprieties adopted in the MARS project (Masi et al. 2021, 2022) for deriving fragility curves relevant to the residential Italian building stock (Lagomarsino and Masi 2021). In particular, the definition of the elastic period is based on the proposal of Pagnini et al. (2011), which

originally referred only to the contribution of the shear stiffness under the hypothesis of shear-type system, with the introduction of some additional correction factors proposed in (Lagomarsino and Cattari 2014) to account for incidence of structural details typical of LQD and HQD configurations.

Figure 3b and c show the variation of the period considering the impact of the presence of LQD or HQD, regular or irregular masonry type, and two types of diaphragms, i.e., flexible (e.g. vaults and timber) or rigid (with reinforced concrete slab). The Figure aims to provide an idea of the plausible range of variations expected for URM buildings. As evident, the wide variety of features that may affect the response of URM buildings (masonry type, structural details, and diaphragms) has a quite significant impact.

Subsequently, the period elongation was computed both without (classical SFSI problem) and with FSFI among footings. For SUs in aggregate with independent but adjacent internal side walls, the number of foundations was set equal to 4, 5 and 6 for building Class 1, 2 and 3, respectively, while *S/B* was varied according to the values reported in Table 3. Interaction with the foundations of neighbouring buildings was also considered, assuming the shortest $S_b/B$.

Figure 4 shows the period changes as a function of $\sigma$ for the three analyzed structural classes. In the first three graphs (Fig. 4a), the period elongation is caused by SFSI, while the next plots show the effect due to cross-interaction FSFI within the same building (Fig. 4b) and with foundations of adjacent buildings (FSFI nearby) (Fig. 4c).

The colored zones in Fig. 4 indicate the variation ranges of the obtained $T^*/T_0$ ratios, with the upper and lower bounds corresponding to the cases reported in the plot. As relative stiffness, $\sigma$, decreases, the range of variability increases. For soils with low shear wave velocities, the σ values for the considered schemes range between 2 and 4. In this region $T^*$ can range from a minimum of about 2 times $T_0$ to a maximum of about 7-8$T_0$. As expected, the effects are more pronounced for building Class 1, which is characterized by the lowest fixed-base period and the largest $\delta$.

The cross-interaction among footings of the same building (Fig. 4b) slightly increases the period elongation, as well as the cross interaction among footings of neighboring buildings (Fig. 4c). Note that 0D-In is based on the replacement oscillator model, which simulates the in-plane response of the structure, hence only considers the translational impedance along X ($K_{xx}$) and the rotational component around Y ($K_{ry}$). Such approximation is widely used in SFSI analyses and is considered reliable because $K_{xx}$ and $K_{ry}$ effectively control the in-plane dynamic response. Anyway, the obtained results should be considered a lower bound of the period elongation due to cross-interaction because they neglect the reduction in $K_{zz}$ and $K_{yy}$, which are significant, as shown in Fig. 2.

Figure 5 shows the variation of the damping ratio, $\beta^*$, with σ, calculated by considering only SFSI. Very similar results are obtained considering FSFI, since the imaginary parts of the impedance functions are minimally affected by cross-interaction (see Zeolla et al. 2024). The upper range of variation (larger coloured area) are obtained assuming the minimum values of *h/B* and maximum values of $\delta$, which leads to an important increase in the damping ratio compared to the fixed base value. Conversely, the minimum values of $\delta$ (and thus the maximum *h/B* values) provide for smaller ranges of variation (lower part of plot), which are even less than the fixed-base damping ratio (3%). The variation in the damping ratio, as well as the maximum value achieved, increases when moving from Class 1 to 2, and from Class 2 to 3.

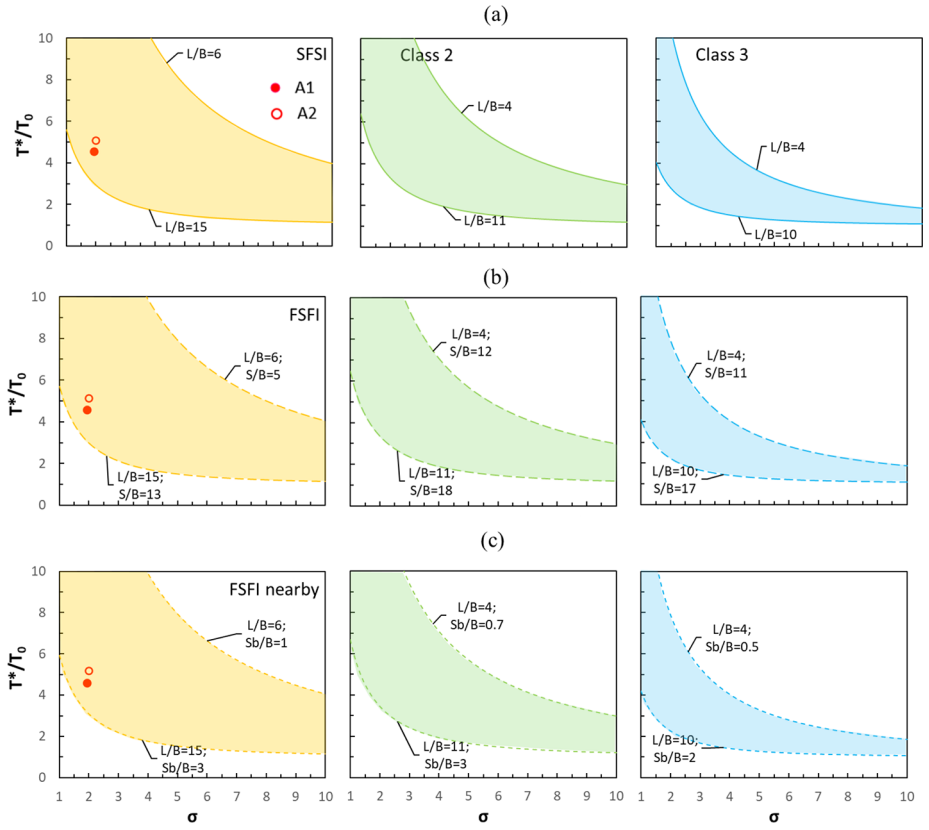


**Fig. 4** Period elongation vs. σ for the three structural classes considered: (**a**) due to SFSI and FSFI between footings of (**b**) the same buildings or (**c**) neighbouring buildings. The range of variation of $T^*/T_0$, highlighted with the coloured areas, is limited at the top and bottom by the curves obtained from the maximum or minimum values of h/B and δ (depending on the class) and the L/B ratios considered (see Table 3)

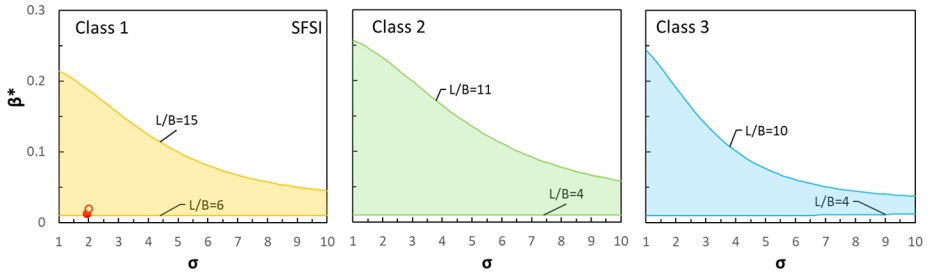


**Fig. 5** Damping ratio vs. σ for the three structural classes considered, due to SFSI

## 3 Application on real URM case studies

As described in previous sections, cross-interaction effects are more pronounced between the foundations of neighbouring buildings due to the shorter distances between them. For this reason, among the three classes introduced in Section § 2.1, this paper focuses on Class 1, analyzing two groups of buildings in aggregate. These buildings are inspired by the building stock of the historic centre of Visso, which was affected by the Central Italy seismic sequence of 2016–2017, and showed evidence of both site and SFSI effects (see Brunelli et al. 2022b).

These structures were studied in three different configurations:

- FB, that is the fixed-base model, in which the structural model is fix at its base and the input motion is calculated through one dimensional site response analyses, considering four different subsoil conditions, whose features are described in Sect. 3.1.
- $CB_{SFSI}$ that is the compliant-base model, endowed at its base with springs calibrated through the impedance function by Gazetas (1991), and characterized by a damping ratio that includes the contribution of the soil.
- $CB_{FSFI}$ that is the compliant-base model, in which the base springs are still calibrated through the impedance function by Gazetas (1991) but modified through the group coefficients by Zeolla et al. (2024) and characterized by a damping ratio that includes the contribution of the soil.

Also, $CB_{SFSI}$ and $CB_{FSFI}$ models are excited by the same input motions of the FB case. The comparison among the results aims to highlight the effect of SFSI (classical interaction) and FSFI (cross interaction).

### 3.1 Description of subsoil conditions and site effects

The input motions for the structural analyses were obtained from linear equivalent site response analyses conducted on the four subsoil profiles shown in Fig. 6.

The first profile (S1) corresponds to the actual soil layer beneath aggregate A2, consisting of a sandy gravel layer (SG) overlaid and locally interbedded with clayey silt (CS) and silty clay (SC) lenses. The shear wave velocity, $V_s$, was measured using MASW and down-hole tests (Cattari et al. 2018b; MZS3, 2018). The free-field frequency, measured on-site through

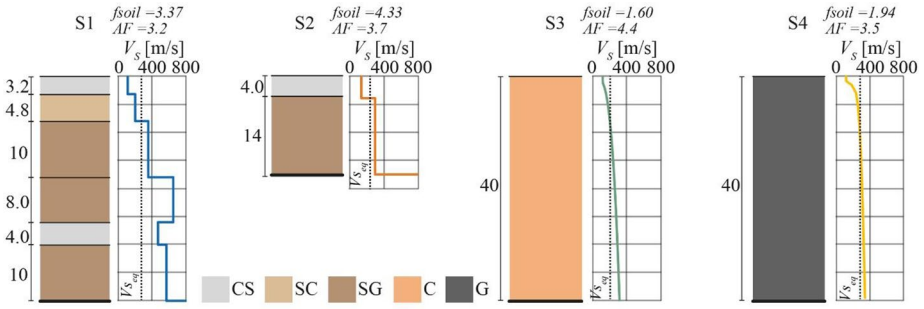


**Fig. 6** Stratigraphy and *Vs* profiles for each subsoil configuration, as adopted in Brunelli et al. (2021a)

HVSR tests, allowed for the back-calculation of the bedrock depth, estimated at 40 m. The shear wave velocity, $V_S$, varies with depth, with an equivalent value of 281 m/s down to the bedrock.

The second profile (S2) represents the actual soil configuration in the historic centre of Visso (near aggregate A1), investigated through two boreholes and an HVSR test (MZS3, 2018). This profile comprises 4 m of clayey silt (CS) over an 11-metre-thick sandy gravel layer (SG). The geological section of the Visso valley, as reported by MZS3 (2018), indicates the bedrock at a depth of 18 m. Since direct measurement of $V_S$ was not available, its value was derived using a correlation law between *Vs* and the number of blows from Standard Penetration Tests conducted at depths of 1.9 m in CS and at 4.4 and 8.9 m in SG. This analysis, detailed in Brunelli et al. (2021a), resulted in an equivalent $V_{Seq}$ value of 272 m/s down to the bedrock.

Additionally, two idealised profiles were considered: one clay-based (S3) and one gravel-based (S4), with bedrock at a depth of 40 m. In both cases, $V_S$ increases with depth. The *Vs* profiles were determined using empirical laws by d'Onofrio and Silvestri (2001) for S3 and by Hardin and Kalinski (2005) for S4. The resulting equivalent $V_{Seq}$ values are 200 m/s and 279 m/s, respectively, which are comparable to those of S1 and S2.

The variation of the normalised shear modulus ($G/G_0$) and damping ratio (D) with shear strain ($\gamma$) for the fine-grained soils in S1, S2, and S3 were derived from a comprehensive model calibrated by Ciancimino et al. (2020) using laboratory test results on similar materials. The $G/G_0$ -$\gamma$ curves for the sandy gravel soil in S1, S2, and S4 were taken from Liao et al. (2013). The corresponding D-$\gamma$ curves were calculated by applying the model of Ramberg and Osgood (1943) and the Masing criteria (Masing 1926) to the $G/G_0$ -$\gamma$ curves.

In addition to the soil layer configurations and $V_S$ values, Fig. 6 presents the soil fundamental frequency ($f_{soil}$) and amplification factor (AF) for each stratigraphy, calculated through a linear site response analysis using STRATA software (Kottke and Rathje 2008). The results show considerable variation in the responses of the four soil profiles, with the maximum AF observed in S3. The site effects for the four soil profiles were subsequently analysed through linear equivalent site response analyses using input motions selected from the Selected Input Motions for Displacement-Based Assessment and Design (SIMBAD) database (Smerzini and Paolucci 2013; Smerzini et al. 2014). The selection included the EW and NS components of accelerations recorded during 49 natural events at stations situated on a stiff rock outcrop ($V_{Seq} > 700$ m/s). The selected signals were slightly scaled (with a scale factor between 0.6 and 1.75) to achieve the desired variability in intensity measures for the construction of fragility curves. For further details, refer to Brunelli et al. (2022a).

Figure 7 shows the mobilized values of normalized stiffness $G/G_0$ (a) and damping D (b), calculated for the four soil profiles through 1D site response analyses. Reference was made to the mean values mobilized within the soil volume likely affected by the foundation motion (i.e., 1 m below the foundation level). As expected, the highest nonlinear effects are observed for profile S4, where stiffness reduction occurs at the earliest, and profile S3, which is characterized by the lowest initial stiffness. Conversely, the lowest degree of nonlinearity is associated with the shallowest bedrock, which produces the highest natural frequency and thus the stiffest response.

Figure 8 illustrates the spectral amplification factor (i.e., the ratio between the spectral acceleration at the ground level, as obtained from the site response analysis, and the input motion) plotted against the spectral acceleration of the input signal, computed at the fun-

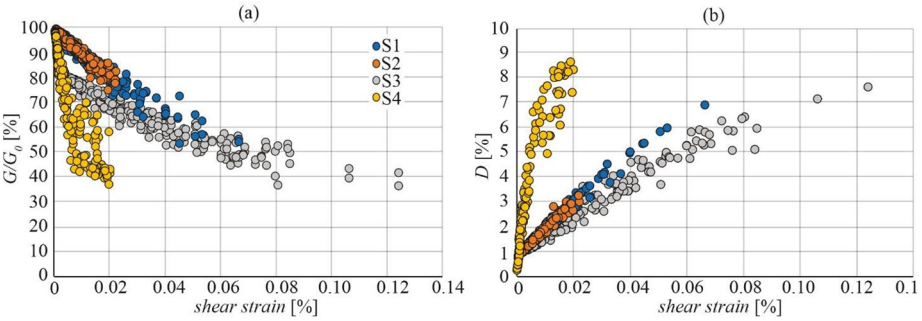


**Fig. 7** Mobilized values of (**a**) $G/G_0$ and (**b**) D the four considered soil profiles under each input motion

damental period of the two aggregates described in Sect. 3.2. Firstly, it is evident that for each model configuration (FB, SFSI, and FSFI), the spectral ratios for a given subsoil are not vertically aligned due to changes in structural periods resulting from soil or foundation-foundation interaction. This variation is particularly noticeable with the introduction of classical soil-structure interaction (FB vs. SFSI), although additional, smaller changes occur when FSFI is also considered, affecting the spectral acceleration values.

In all cases, the amplification factors decrease with increasing input motion spectral acceleration, highlighting the expected contribution of site effects. For higher input motion accelerations, models with SFSI and FSFI exhibit higher amplification factors compared to the FB model. This general trend is more or less pronounced depending on the subsoil considered. Therefore, Fig. 8 demonstrates the anticipated reduction in amplification with increasing input motion amplitude. This effect is beneficial for structural safety, as strong motion events are less amplified by site effects.

Conversely, SFS interaction shifts the structural period towards the predominant soil period, where spectral ordinates are maximized. As a result, higher spectral accelerations affect the coupled model with interactions, except for very weak motions, particularly for soil S1 (around $Sa < 0.25$ g).

Changing the spectral acceleration of the input in the nonlinear dynamic analysis is one of the factors that can alter the expected damage outcomes. It should be noted that other factors, such as variations in the damping of the analysis and changes in the stiffness of the base constraints, as discussed in previous chapters, also contribute to these changes.

### 3.2 Mean feature and modeling assumptions

Both URM buildings in aggregate here investigated are composed of five structural units, but only three were analyzed in detail for the first (A1) and for the second (A2). The latter has been demolished due to the severe damage occurred in some SUs after the 2016–2017 seismic event. Figure 9 shows the ground floor plans of the two examined configurations and an overview photo. The two configurations are characterized by structural slenderness ratio, $h/B$, of 28.9 and 15.5, and structure-to-soil relative mass, $\delta$, of 227 and 331, respectively. These ratios were obtained by considering the maximum height values between the different structural units and the average values of the half-width between the foundations in the buildings in aggregate. The resulting values are within the maximum and minimum val-

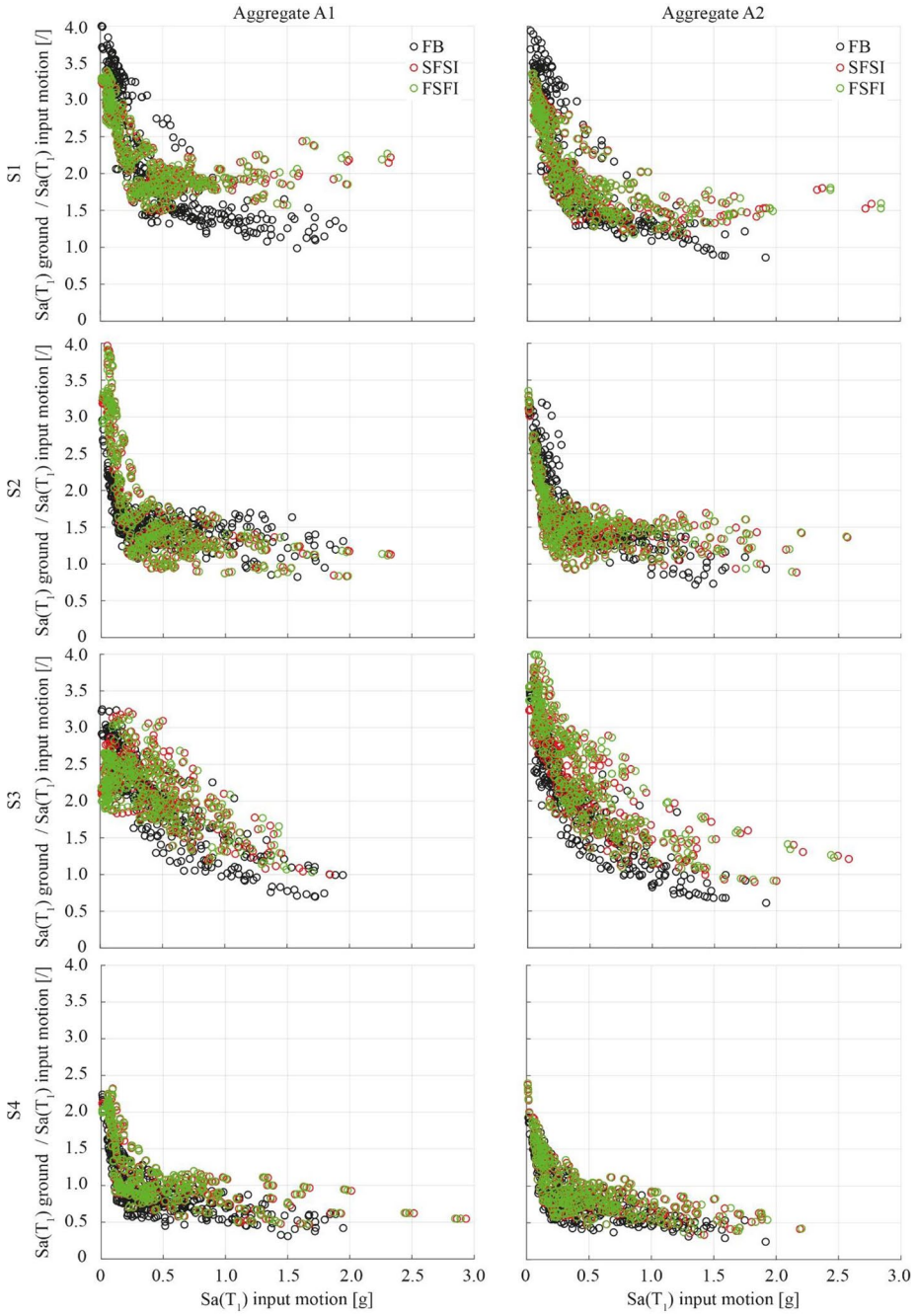


**Fig. 8** Ground-to-input motion spectral amplification factors vs. Sa ($T_1$) of the input signal for the two aggregates and the four soil profiles

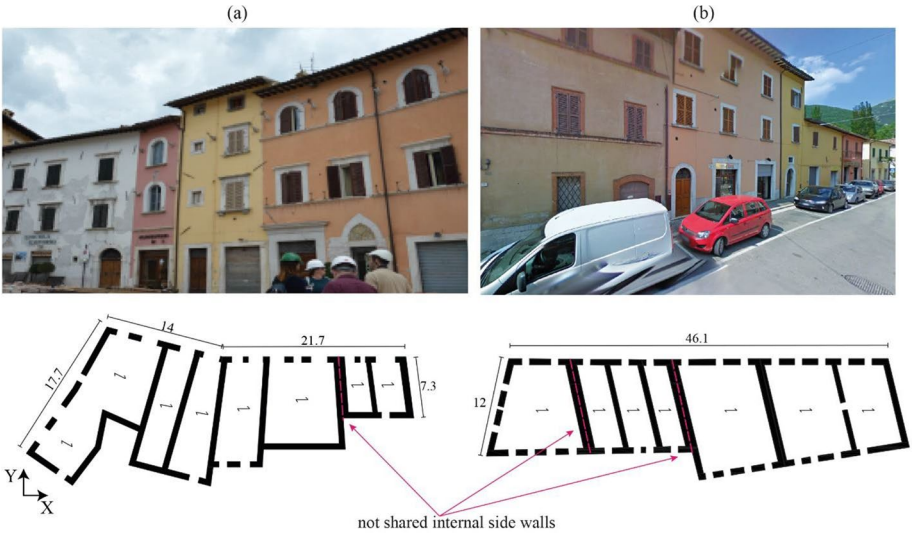


**Fig. 9** Plans and photo of the two considered aggregate: (**a**) A1 and (**b**) A2

ues obtained for Class 1 (see Table 3). The characteristics of the two buildings in aggregate are similar: the walls were estimated to be 70 cm thick at the ground floor and 60 cm at the other levels. The only exception is the perimeter wall of unit $U1_{A1}$ (the right wall in Fig. 9a) estimated 80 cm thick over the entire height of the building. Moreover, the presence of internal walls was assumed in correspondence with the tie-rods visible in the external façades. The internal walls were supposed 5 cm lower as thickness than the relative perimeter walls. Unit $U4_{A1}$ seems to be a filling unit built upon the two pre-existing orthogonal walls.

The main orientation of diaphragms is expected to develop perpendicularly to the Y-direction. The same floor with a concrete slab (not reinforced) was assumed in all units of the aggregate under examination since there is no evidence of any specific interventions and the units are considered substantially contemporary. Both configurations consist of foundation walls with an average width, 2B = 0.8 m, and an average length, 2L = 9 m, so the *L/B* ratio is about 10. In A1, which is the most irregular with very elongated sides (Fig. 9a), the minimum distances, S, between the foundations vary from 3.3 to 6.6 m, while in A2 (Fig. 9b), which is more regular in plan with sides of similar length, S vary between 3 and 5.8 m. Figure 2(c) shows the values of the dimensionless ratios between the stiffness of the foundation in group and alone, related to the foundations of the two aggregates considered. Note that only the dimensionless ratio along Z (vertical) and X (long side of the foundations) and rotational around Y have been reported, as these are the ones included in the equivalent frame numerical model described later in Sect. 3.2. The ratios for the three degree of Freedom were calculated using the $a_i$ and $b_i$ coefficients for two nearby foundations (third column in Table 2) and the superposition principle, because the distances of the foundations inside the building are not equal. In fact, the indicators related to the internal foundations (see filled indicators) are not perfectly aligned on the black curves. While $K_{ry}$ rotational stiffnesses are reduced negligibly, vertical and horizontal stiffness ($K_{zz}$ and $K_{xx}$) can be reduced by as much as 18–20% when *S/B* are lower. To estimate the changes in period and damping due SFSI and FSFI, the soil-to-structure relative stiffness, $\sigma$, was calculated using

the $V_S$ = 136 m/s and $V_S$ = 162 m/s respectively corresponding to the shallowest soil layer in S1 for A2 and S2 for A1. The assumed $V_S$ values correspond to $G_0$ respectively equal to 3.7 MPa and 5.3 MPa, used to calibrate the analytical impedance functions joint to a Poisson coefficient equal to 0.33.

The fixed-base period, $T_0$, in the Y-direction was 0.14 for A1 and 0.098 for A2. The period $T^*$ is about 4 $T_0$ and 3 $T_0$ for A1 and A2 respectively, while the damping ratio $\beta^*$ is about 1% and 2%, thus below the fixed-base damping. Note that this initial value is calculated considering only the foundation radiation damping ratio and neglecting the hysteretic contribution of the soil. These results are depicted with red dots (full for A1 and empty for A2) in Figs. 4 and 5.

The structural model – illustrated in Fig. 10a - was developed according to the equivalent frame (EF) modeling approach implemented in the Tremuri software (Lagomarsino et al. 2013). According to the EF approach each wall is discretized in piers (vertical URM elements), spandrels (horizontal URM elements), and rigid areas (nodes); the indication of the SUs investigated in detail through the NLDAs is also reported. More specifically, the piecewise-linear beam model has been assumed to describe the nonlinear response of URM panels (Cattari and Lagomarsino 2013; Cattari et al. 2018a). This constitutive law describes the nonlinear response until very severe damage levels ($DL_E$, from 1 to 5), through the definition of a relation between the drift value $\delta_{E,i}$ and the corresponding value of the residual shear strength $\beta_{E,i}$ at the attainment of the i-th DL. The values of $\delta_{E,I}$ and $\beta_{E,i}$ are differentiated for piers and spandrels and also varying the prevailing failure mode, i.e. if flexural or shear or hybrid (see for example Fig. 10b). The initial stiffness is defined according to the beam theory while the maximum strength is computed according to some criteria well recognized in literature for interpreting the failure modes aforementioned (i.e. for the flexural response that also adopted in Codes (NTC 2018; CEN 2004) while for the shear one the one proposed by Turnsek and Cacovic (1971). The mechanical parameters adopted are reported in Table 4 and are consistent with the assumptions already tested and verified in Brunelli et al. (2022c), where a detailed simulation of the actual response of two configurations subjected to the real seismic event has been investigated. While the reliability of the adopted numerical approach (both considering the FB and CB models) was already proven by the validation provided on the monitored school building of Visso in Brunelli et al. (2021b), the further numerical investigation on these configurations demonstrated its effectiveness also in assessing the response of SUs in aggregate. According to the approach introduced by Angiolilli et al. (2023), the interaction effect between adjacent units was modeled introduc-

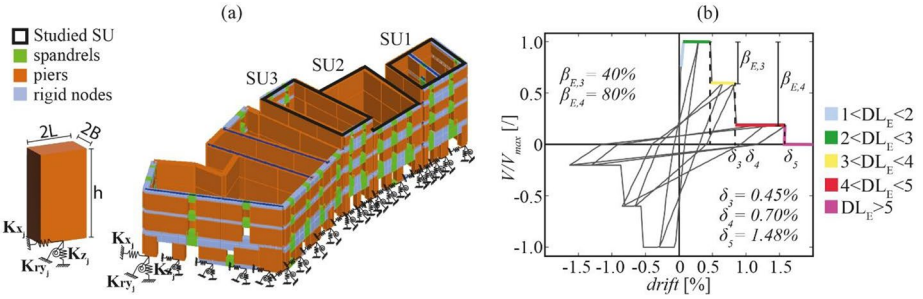


**Fig. 10** (**a**) 3D equivalent frame model of the aggregate A1 and example of pier with springs (**b**) backbone and hysteretic response of piers under shear force

**Table 4** Mechanical parameters adopted for structures

| | Aggregate A1 | | | | Aggregate A2 | | | |
|---|---|---|---|---|---|---|---|---|
| | E (MPa) | G (MPa) | $\tau_0$ (MPa) | $f_m$ (MPa) | E (MPa) | G (MPa) | $\tau_0$ (MPa) | $f_m$ (MPa) |
| Piers | 2968 | 991 | 0.127 | 6.42 | 2574 | 858 | 0.641 | 4.94 |
| Spandrels | 2078 | 693 | 0.062 | 4.49 | 1800 | 741 | 0.641 | 3.80 |

ing a finite-length gap and, then, connected by elastic truss elements (sectional area of 16.4 $cm^2$ and elastic modulus E of 210000 MPa with null tensile behaviour) as well as fictitious floors (thickness of 0.05 m, E = 39420 MPa, G = 13112 MPa).

In the analyses considering the SFSI, each pier of the structural model was equipped with springs, restraining the translation along the in-plane horizontal ($K_x$) and vertical ($K_z$) directions and to the rocking ($K_{ry}$) around the axis parallel to the foundation width. The spring stiffness was calibrated through the real part of the soil-foundation impedances (Gazetas 1991). The foundation shape varies from square to rectangular being the foundation length defined by adding the half-length of the spandrel panel to the size of the load-bearing wall. Conversely, the foundation width is equal to 1 m, as a result from the thickness of the load-bearing wall plus an enlargement of 0.15 m at each side. The value of the embedment was set to 1 m.

The calibration of the impedance was performed considering the mean shear modulus mobilized in the soil volume affected by the foundation motion, under each input motion as shown in Fig. 7. For each case, the frequency-dependent dynamic coefficients of the impedances were computed as a function of the fundamental period computed through the-Maravas et al. (2014) formulation. The calibration was solved iteratively until the resulting period was equal to the value adopted in the impedance function computation.

In the analyses considering FSFI, the impedances were modified through the coefficients proposed by Zeolla et al. (2023).

The imaginary part, which quantifies the radiation damping, was divided by the double of the real part of the impedance to obtain the energy loss coefficients $\beta_x$, $\beta_z$ and $\beta_{ry}$. The latter was introduced in the formula by Maravas et al. (2014) to calculate the equivalent damping ratio of the soil-foundation-structure system, together with the structural viscous damping ratio $\beta_0 = 3\%$ and the mean soil hysteretic damping mobilized under each input motion reported in Fig. 7. The resulting value was introduced as an equivalent Rayleigh damping ratio in the structural analysis. Due to soil hysteresis, the interaction always increases the fixed-base damping, reaching values up to 4 times larger. The increase due to FSFI is a further 4 to 5 per cent compared to traditional interaction.

### 3.3 Procedure adopted for deriving the fragility curves

Fragility curves according to a lognormal format have been derived for Damage Levels (DLs), aimed to be conceptually consistent with the definitions proposed in the European Macroseismic Scale (EMS98 - Grünthal 1998). To this aim, the procedure described in Brunelli et al. 2022a has been adopted. Depending on the maximum damage achieved, the analyses were grouped into the 6 DLs classified as proposed by EMS98: DL0 - none, DL1 - negligible, DL2 - moderate, DL3 - severe, DL4 - very severe to near collapse and DL5 – collapse. The average value ($PGA_{mi}$) and the standard deviation ( $\sigma_{mi}$) of the Peak Ground Acceleration (PGA) of the input motions causing the achievements of each damage

level, $DL_i$, was then calculated. They were used to calibrate a lognormal distribution of the PGA causing the attainment of $DL_i$. According to this procedure, the results of records can be divided in group in function of the global DL. The probability of exceeding the different damage levels, $p_{DLi}$, under a certain PGA can be consequently calculated as the probability that such PGA "exceeds" the calibrated lognormal distribution:

$$p_{\mathrm{DL}_i} = p(\mathrm{DL} > \mathrm{DL}_i \mid \mathrm{PGA}) = \Phi\left(\frac{\log\left(\frac{\mathrm{PGA}}{\mathrm{PGA}_{mi}}\right)}{\sigma}\right) \tag{5}$$

where Φ is the standard cumulative probability function. The value of the standard deviation accounts for the record-to-record variability contribution and the uncertainty associated with the definition of DL. The attainment of a specific DL accounts for multiscale approach based on the severity of the damage occurred in URM panels, on the spread of the damage along the structure (Cattari and Angiolilli 2022).

Figure 11 presents the fragility curves for A1 based on soil profile S1. The whole set of fragility curves is reported in Annex I along with a table with $PGA_{mi}$ values. As shown in Fig. 11, soil structure interaction shifts the curves to the right (indicating lower vulnerability) compared to the FB model. The difference between the $CB_{SFSI}$ and $CB_{FSFI}$ models is relatively small, with the greatest impact associated to more severe DLs. This result depends on various factors, such as the period elongation, which leads to different spectral acceleration (as shown in Fig. 8), but also to different values of the equivalent damping provided by the Maravas formulation.

## 4 Discussion on the overall set of results from NLDA

This section aims to provide a comprehensive overview of the main findings obtained by the whole set of NLDAs carried out and fragility curves when varying the soil profiles, SUs configurations and the three models considered.

Firstly, for each DL, Fig. 12 shows the so-called Modification Factor (MF), which is the ratio between the median $PGA_{50}$ obtained from the $CB_{SFSI}$ and FB models (grey markers) or $CB_{FSFI}$ and FB models (black markers), respectively. The figure shows the MF obtained for each SU studied, for the two examined buildings in aggregate. It should be noted that where

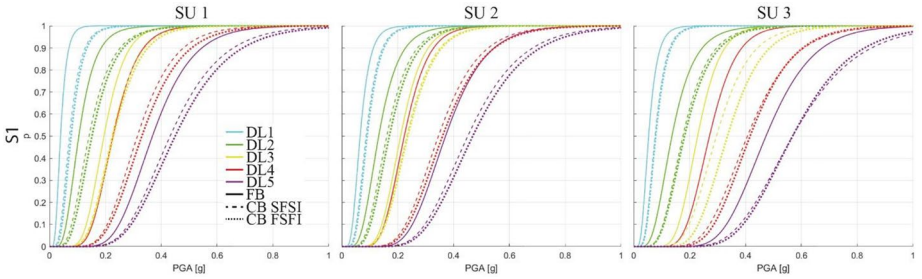


**Fig. 11** Fragility curves for the A1 SU with soil profile S1 and considering the FB model (with site amplification only), the $CB_{SFSI}$ model (with soil-structure interaction) and the $CB_{FSFI}$ model (soil and cross interaction between the nearby foundations)

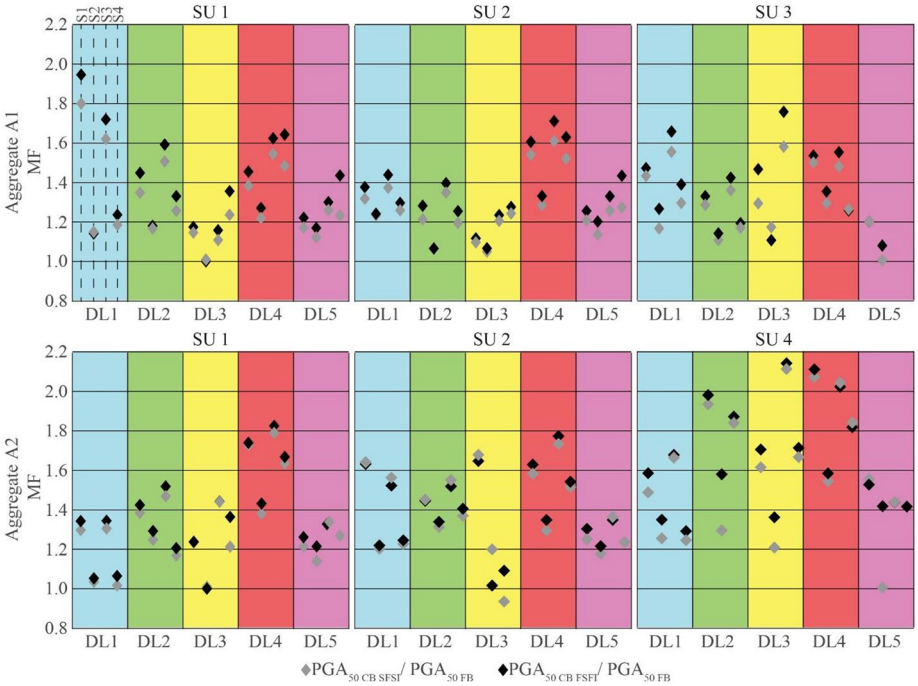


**Fig. 12** Ratios between the $PGA_{mi}$ obtained from the compliant and fixed base models for the analysed structural units of the two aggregated buildings in as DLs change

the statistical value is considered unreliable (see tables in the Annex 1 for each fragility curve), the value has not been reported in Fig. 12.

The two models with soil-structure interaction ($CB_{SFSI}$, $CB_{FSFI}$) are almost always less vulnerable than the fixed-base model, as the MF parameter usually falls within a range of 1.2 and 1.6, or is in any case greater than 1. In certain cases (3 for A1 and 3 for A2), the MF value is close to 1, and in only one DL for A2 it is less than 1 (for $CB_{SFSI}$). Only in some cases the two compliant base models are associated with a larger scaling factor MF, especially for the model that accounts also for the cross interaction. However, the differences are not always associated with a specific soil profile or a given DL, so that no clear and unambiguous trend may be seen. The differences in damping between the three models, shown in Fig. 8, are not always directly related to the larger (or smaller) differences shown in Fig. 12 since this latter figure is the synthesis of multiple parameters: the shape and intensity of the bidirectional input accelerograms, the directional vulnerability of the building, the mobilized period, the signal spectrum, the damage attribution criterion, the modification of each foundation pier's impedances with FSFI etc. The same input analysis yields a different effect across the various structural units in the same aggregated building, depending on two parameters: the vulnerability of each individual structural unit in comparison with the others; and the different impedance value at the base of each masonry pier, which can further vary from unit to unit due to FSFI, depending on the distances *S* between the internal masonry piers. This demonstrates the complexity of the problem analyzed and the numerous factors that influence the structural response.

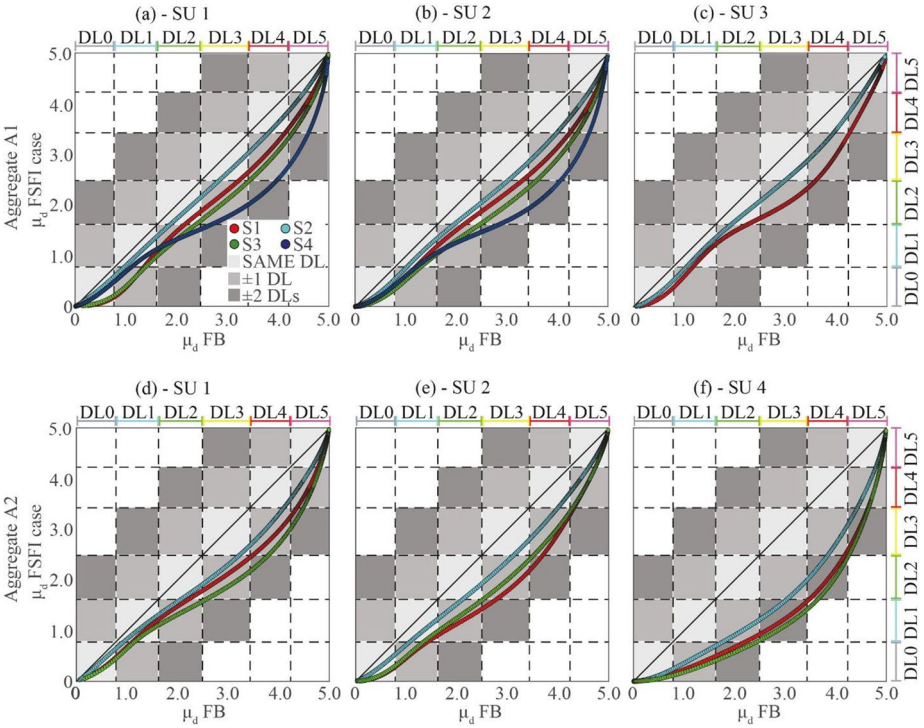


**Fig. 13** Comparison among the $\mu_d$ resulting from the different analysed SUs from the curves expressed as a function of PGA

To better study the effects in terms of statistical response of structure using the fragility curves, a summary parameter called mean damage $\mu_d$ was used. This parameter describes the mean statistical damage of structure that occurs after a seismic event. It is calculated through Eq. 6:

$$\mu_d = \sum_{i=0}^{5} (p_{DLi}\, i) \tag{6}$$

where $p_{DLi}$ is weighted by i=0,1,2,3,4 or 5 passing from DL0 to DL5.

The calculation was performed by entering in each fragility curve (of three models) with the values of PGA at the bedrock of each selected input motion. The $\mu_d$ value may be conveniently converted into an equivalent discrete damage level by assuming a binominal distribution, leading to the following conversion intervals (Lagomarsino and Giovinazzi 2006): 0-0.7 for DL0; 0.7–1.6 for DL1; 1.6–2.5 for DL2; 2.5–3.4 for DL3; 3.4–4.3 for DL4; 4.3-5 for DL5. This type of graphical representation was already used in another paper of Authors (see e.g. Brunelli et al. 2022a). This conversion intervals are used to define the "square metric" in Fig. 13. The grey fillings indicate a difference of 1 or 2 DLs between the mean damage of FB and complaint base model. The bisector dividing the area into two regions is also shown, with the area above indicating greater damage in the model with the interaction, and the area below indicating greater damage in the fixed-base model. As the conversion is based on a range of variations, there is a region (light grey rectangles) where

the two models have the same $\mu_d$. Since it was already noted that for the two interaction models (SFSI and FSFI) the differences were minimal, only the comparison between the $\mu_d$ of the FB model (on the X-axis) and the model $\mu_d$ with cross interaction FSFI (on the Y-axis) was depicted in Fig. 13.

The model with only site amplification (FB) has a significant overestimation of damage, even 2 and 3 DLs (see e.g. Figure 13a, b with soil S4 or Fig. 13f for all soils). This result has been confirmed by all examined soil profiles and structural units for the two buildings in aggregate. Only in some cases, the differences are smaller, especially in the case of S2 for all the units except for SU 4 of A2 (see Fig. 13f). However, in all cases, the model with the SFSI reduces the expected damage, and never leads to an overestimation of the damage.

## 5 Conclusions

The seismic performance of a building aggregate can be influenced by foundation-soil-foundation interaction (FSFI), in addition to standard soil-foundation-structure interaction (SFSI) and site effects (SE). While several approaches exist in the literature to address these issues for standalone constructions, buildings in aggregates are often modeled as isolated and fixed at their base. This paper investigates the effects of SFSI and FSFI on the period and damping ratio estimates of typical URM buildings for the development of fragility curves.

Three structural classes of masonry buildings, typical of Italian and European heritage, were identified. The reduction in static stiffness due to the proximity of the foundations of both the same and neighboring buildings was then estimated.

Translational motions of the foundations are most affected by the interaction with the soil and neighboring foundations through the shared soil. The lowest stiffness values are obtained for the horizontal degree of freedom along the y-axis (almost 20% less than in the case of isolated foundations), which corresponds to the direction along which the footings are aligned, especially when they are located inside the building (central footings).

Residential masonry buildings in aggregate, which are typical of small historical centres, constitute the class that experiences the greatest reduction in stiffness because their foundations are characterized by smaller *S/B* ratios and, consequently, higher reduction coefficients due to group effects. Conversely, structural classes with higher *S/B* ratios in their foundations experience a smaller, albeit non-negligible, reduction in stiffness.

For the building classes considered, the period and damping variation from the fixed base condition have been evaluated. The results are grouped into spindles showing the range of period variability, for different building classes, as the foundation shape ratio, *L/B*, changes. When the interaction is considered, the spindle shifts upward (higher periods) and the difference between $T^*$ and $T_0$ increases when the presence of nearby buildings is included.

Subsequently, the paper analyzed two representative buildings in aggregate inspired by the historic center of Visso, investigating three different configurations: the Fixed Base (FB) model, which only considers site amplification; the Compliant Base (CB) model, which incorporates structure-soil interaction (SFSI); and a configuration that includes the additional contribution from foundation-soil-foundation interaction (FSFI).

NLDAs were performed with input accelerograms obtained from local seismic responses for four soil profiles. The analyses were then divided according to the maximum damage

obtained with that accelerogram, and the fragility curve was computed for DLs compatible with the EMS98 definitions for the three models. The fixed-base model overestimates the probability of failure. In particular, the ratio of the median value of the fragility curves obtained from the compliant base (SFSI or FSFI) models and that obtained from the fixed base model ranges between 1.2 and 1.6. The results of the cross-interaction models showed slightly higher values than those considering only the SFSI. In some cases, the two formulations differed more, with a higher scaling factor for the foundation-foundation interaction model. However, although there is a noticeable reduction in stiffness at the base of the masonry units, the additional contribution of the footing-footing interaction has a modest impact on the fragility curves, at least for the case studies examined to date. What is clear is that when considering the model with site amplification only, for almost all the subsoil profiles and structural units considered, there is a significant overestimation of the expected damage compared to the actual one, even by 2–3 DL. In a few cases the differences are smaller. On the contrary, the model with foundation-to-foundation interaction (FSFI) reduces the expected damage and never leads to an overestimation. The model with SFSI (traditional) leads to the same results, although it normally lies somewhere in between the other two models considered.

## 6 Annex I

Tables with median values ($IM_{50}$) and deviations ($\sigma$) for each modelling and soil configuration for the different structural units of the two aggregates are shown. In the case of an analysis value of less than 10, the fragility curves are not reported as they are considered to have low statistical robustness.

Building in Aggregate A1.

**Table 1** Annex: value of fragility curves for A1 and soil S1

| | | SU1 | | | SU2 | | | SU3 | | |
|---|---|---|---|---|---|---|---|---|---|---|
| | | $IM_{50}$ [g] | σ | N analyses | $IM_{50}$ [g] | σ | N analyses | $IM_{50}$ [g] | σ | N analyses |
| FB C | DL1 | 0.040 | 0.443 | 27 | 0.066 | 0.427 | 47 | 0.053 | 0.458 | 51 |
| | DL2 | 0.105 | 0.443 | 128 | 0.132 | 0.427 | 110 | 0.137 | 0.458 | 138 |
| | DL3 | 0.195 | 0.307 | 23 | 0.210 | 0.301 | 23 | 0.229 | 0.278 | 20 |
| | DL4 | 0.227 | 0.307 | 55 | 0.224 | 0.301 | 42 | 0.271 | 0.278 | 76 |
| | DL5 | 0.369 | 0.307 | 100 | 0.371 | 0.301 | 97 | 0.473 | 0.278 | 46 |
| CB SFSI | DL1 | 0.071 | 0.454 | 49 | 0.087 | 0.408 | 47 | 0.076 | 0.408 | 55 |
| | DL2 | 0.142 | 0.454 | 113 | 0.161 | 0.408 | 104 | 0.176 | 0.408 | 169 |
| | DL3 | 0.224 | 0.329 | 43 | 0.232 | 0.325 | 52 | 0.296 | 0.316 | 11 |
| | DL4 | 0.315 | 0.329 | 75 | 0.346 | 0.325 | 64 | 0.407 | 0.316 | 71 |
| | DL5 | 0.432 | 0.329 | 33 | 0.451 | 0.325 | 25 | 0.569 | 0.316 | 2 |
| CB FSFI | DL1 | 0.077 | 0.432 | 54 | 0.091 | 0.398 | 47 | 0.078 | 0.411 | 55 |
| | DL2 | 0.152 | 0.432 | 113 | 0.170 | 0.398 | 114 | 0.182 | 0.411 | 170 |
| | DL3 | 0.229 | 0.337 | 40 | 0.236 | 0.325 | 43 | 0.335 | 0.292 | 9 |
| | DL4 | 0.331 | 0.337 | 80 | 0.361 | 0.325 | 65 | 0.416 | 0.292 | 66 |
| | DL5 | 0.450 | 0.337 | 22 | 0.469 | 0.325 | 19 | 0.569 | 0.292 | 2 |

**Table 2** Annex: Value of fragility curves for A1 and soil S2

| | | SU1 | | | SU2 | | | SU3 | | |
|---|---|---|---|---|---|---|---|---|---|---|
| | | $IM_{50}$ [g] | σ | N analyses | $IM_{50}$ [g] | σ | N analyses | $IM_{50}$ [g] | σ | N analyses |
| FB C | DL1 | 0.070 | 0.453 | 74 | 0.082 | 0.420 | 72 | 0.071 | 0.461 | 82 |
| | DL2 | 0.136 | 0.453 | 92 | 0.166 | 0.420 | 83 | 0.162 | 0.461 | 118 |
| | DL3 | 0.230 | 0.313 | 23 | 0.217 | 0.298 | 22 | 0.230 | 0.286 | 20 |
| | DL4 | 0.236 | 0.313 | 52 | 0.238 | 0.298 | 45 | 0.303 | 0.286 | 69 |
| | DL5 | 0.387 | 0.313 | 85 | 0.397 | 0.298 | 80 | 0.490 | 0.286 | 36 |
| CB SFSI | DL1 | 0.080 | 0.452 | 83 | 0.102 | 0.423 | 66 | 0.083 | 0.432 | 74 |
| | DL2 | 0.159 | 0.452 | 81 | 0.179 | 0.423 | 82 | 0.180 | 0.432 | 145 |
| | DL3 | 0.220 | 0.301 | 37 | 0.230 | 0.315 | 37 | 0.271 | 0.314 | 13 |
| | DL4 | 0.287 | 0.301 | 64 | 0.309 | 0.315 | 58 | 0.393 | 0.314 | 71 |
| | DL5 | 0.434 | 0.301 | 49 | 0.455 | 0.315 | 39 | 0.487 | 0.314 | 7 |
| CB FSFI | DL1 | 0.079 | 0.440 | 80 | 0.102 | 0.416 | 61 | 0.090 | 0.439 | 74 |
| | DL2 | 0.161 | 0.440 | 86 | 0.179 | 0.416 | 88 | 0.185 | 0.439 | 143 |
| | DL3 | 0.220 | 0.282 | 39 | 0.234 | 0.309 | 37 | 0.256 | 0.283 | 15 |
| | DL4 | 0.299 | 0.282 | 61 | 0.320 | 0.309 | 61 | 0.411 | 0.283 | 66 |
| | DL5 | 0.452 | 0.282 | 44 | 0.482 | 0.309 | 32 | 0.531 | 0.283 | 5 |

**Table 3** Annex: Value of fragility curves for A1 and soil S3

| | | SU1 | | | SU2 | | | SU3 | | |
|---|---|---|---|---|---|---|---|---|---|---|
| | | $IM_{50}$ [g] | σ | N analyses | $IM_{50}$ [g] | σ | N analyses | $IM_{50}$ [g] | σ | N analyses |
| FB C | DL1 | 0.045 | 0.388 | 32 | 0.063 | 0.425 | 34 | 0.054 | 0.429 | 41 |
| | DL2 | 0.105 | 0.388 | 107 | 0.129 | 0.425 | 108 | 0.135 | 0.429 | 138 |
| | DL3 | 0.206 | 0.331 | 27 | 0.197 | 0.326 | 26 | 0.225 | 0.270 | 8 |
| | DL4 | 0.211 | 0.331 | 38 | 0.212 | 0.326 | 20 | 0.262 | 0.270 | 88 |
| | DL5 | 0.339 | 0.331 | 123 | 0.340 | 0.326 | 122 | 0.474 | 0.270 | 48 |
| CB SFSI | DL1 | 0.073 | 0.401 | 46 | 0.087 | 0.383 | 46 | 0.084 | 0.413 | 45 |
| | DL2 | 0.158 | 0.401 | 116 | 0.174 | 0.383 | 116 | 0.184 | 0.413 | 164 |
| | DL3 | 0.227 | 0.330 | 33 | 0.238 | 0.340 | 31 | | | 2 |
| | DL4 | 0.325 | 0.330 | 65 | 0.343 | 0.340 | 57 | 0.389 | 0.340 | 78 |
| | DL5 | 0.426 | 0.330 | 37 | 0.429 | 0.340 | 33 | | | 0 |
| CB FSFI | DL1 | 0.078 | 0.394 | 51 | 0.091 | 0.386 | 47 | 0.090 | 0.410 | 41 |
| | DL2 | 0.167 | 0.394 | 123 | 0.180 | 0.386 | 127 | 0.193 | 0.410 | 171 |
| | DL3 | 0.238 | 0.329 | 29 | 0.244 | 0.319 | 24 | 0.396 | 0.319 | 2 |
| | DL4 | 0.342 | 0.329 | 66 | 0.364 | 0.319 | 64 | 0.408 | 0.319 | 68 |
| | DL5 | 0.440 | 0.329 | 29 | 0.454 | 0.319 | 21 | | | 0 |

**Table 4** Annex: Value of fragility curves for A1 and soil S4

| | | SU1 | | | SU2 | | | SU3 | | |
|---|---|---|---|---|---|---|---|---|---|---|
| | | $IM_{50}$ [g] | σ | N analyses | $IM_{50}$ [g] | σ | N analyses | $IM_{50}$ [g] | σ | N analyses |
| FB C | DL1 | 0.103 | 0.467 | 88 | 0.128 | 0.410 | 59 | 0.107 | 0.451 | 85 |
| | DL2 | 0.203 | 0.467 | 92 | 0.230 | 0.410 | 97 | 0.238 | 0.451 | 119 |
| | DL3 | 0.297 | 0.277 | 32 | 0.325 | 0.265 | 16 | 0.358 | 0.248 | 3 |
| | DL4 | 0.300 | 0.277 | 15 | 0.314 | 0.265 | 9 | 0.424 | 0.248 | 54 |
| | DL5 | 0.431 | 0.277 | 53 | 0.431 | 0.265 | 53 | 0.586 | 0.248 | 2 |

**Table 4** Annex: Value of fragility curves for A1 and soil S4

| | | SU1 | | | SU2 | | | SU3 | | |
|---|---|---|---|---|---|---|---|---|---|---|
| | | $IM_{50}$ [g] | σ | N analyses | $IM_{50}$ [g] | σ | N analyses | $IM_{50}$ [g] | σ | N analyses |
| CB SFSI | DL1 | 0.122 | 0.440 | 70 | 0.161 | 0.379 | 67 | 0.139 | 0.404 | 68 |
| | DL2 | 0.255 | 0.440 | 128 | 0.275 | 0.379 | 115 | 0.279 | 0.404 | 158 |
| | DL3 | 0.367 | 0.255 | 20 | 0.404 | 0.233 | 17 | | | 0 |
| | DL4 | 0.445 | 0.255 | 18 | 0.478 | 0.233 | 16 | 0.537 | 0.235 | 13 |
| | DL5 | 0.532 | 0.255 | 8 | 0.550 | 0.233 | 4 | | | 0 |
| CB FSFI | DL1 | 0.128 | 0.427 | 76 | 0.166 | 0.381 | 71 | 0.149 | 0.402 | 63 |
| | DL2 | 0.270 | 0.427 | 135 | 0.289 | 0.381 | 124 | 0.285 | 0.402 | 157 |
| | DL3 | 0.403 | 0.244 | 14 | 0.414 | 0.183 | 9 | | | 0 |
| | DL4 | 0.493 | 0.244 | 17 | 0.512 | 0.183 | 14 | 0.535 | 0.185 | 9 |
| | DL5 | 0.619 | 0.244 | 2 | 0.619 | 0.183 | 2 | | | 0 |

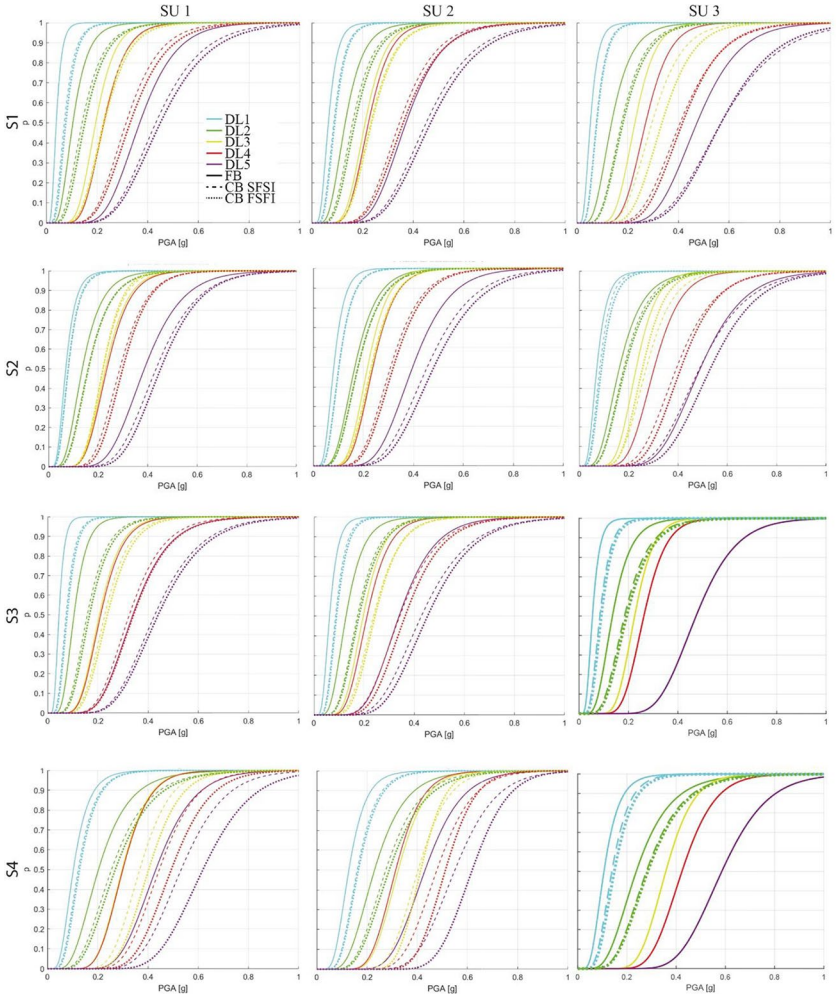


**Fig. 1** Annex: Fragility curves for A1

Building in aggregate A2.

**Table 5** Annex: Value of fragility curves for A2 and soil S1

| | | SU1 | | | SU2 | | | SU4 | | |
|---|---|---|---|---|---|---|---|---|---|---|
| | | $IM_{50}$ [g] | σ | N analyses | $IM_{50}$ [g] | σ | N analyses | $IM_{50}$ [g] | σ | N analyses |
| FB C | DL1 | 0.042 | 0.451 | 29 | 0.052 | 0.439 | 56 | 0.078 | 0.404 | 65 |
| | DL2 | 0.104 | 0.451 | 125 | 0.128 | 0.439 | 95 | 0.117 | 0.404 | 32 |
| | DL3 | 0.190 | 0.318 | 14 | 0.150 | 0.341 | 12 | 0.160 | 0.353 | 30 |
| | DL4 | 0.223 | 0.318 | 55 | 0.203 | 0.341 | 66 | 0.195 | 0.353 | 61 |
| | DL5 | 0.354 | 0.318 | 110 | 0.363 | 0.341 | 104 | 0.339 | 0.353 | 123 |
| CB SFSI | DL1 | 0.054 | 0.483 | 61 | 0.085 | 0.397 | 107 | 0.116 | 0.386 | 143 |
| | DL2 | 0.145 | 0.483 | 138 | 0.185 | 0.397 | 85 | 0.226 | 0.386 | 42 |
| | DL3 | 0.235 | 0.313 | 54 | 0.251 | 0.369 | 5 | 0.258 | 0.305 | 50 |
| | DL4 | 0.385 | 0.313 | 66 | 0.320 | 0.369 | 106 | 0.405 | 0.305 | 60 |
| | DL5 | 0.429 | 0.313 | 15 | 0.453 | 0.369 | 16 | 0.528 | 0.305 | 7 |
| CB FSFI | DL1 | 0.056 | 0.468 | 64 | 0.085 | 0.418 | 103 | 0.124 | 0.401 | 135 |
| | DL2 | 0.149 | 0.468 | 137 | 0.184 | 0.418 | 92 | 0.232 | 0.401 | 44 |
| | DL3 | 0.236 | 0.303 | 53 | 0.246 | 0.359 | 8 | 0.273 | 0.309 | 48 |
| | DL4 | 0.387 | 0.303 | 63 | 0.330 | 0.359 | 100 | 0.412 | 0.309 | 57 |
| | DL5 | 0.446 | 0.303 | 16 | 0.473 | 0.359 | 14 | 0.519 | 0.309 | 6 |

**Table 6** Annex: Value of fragility curves for A2 and soil S2

| | | SU1 | | | SU2 | | | SU4 | | |
|---|---|---|---|---|---|---|---|---|---|---|
| | | $IM_{50}$ [g] | σ | N analyses | $IM_{50}$ [g] | σ | N analyses | $IM_{50}$ [g] | σ | N analyses |
| FB C | DL1 | 0.065 | 0.504 | 66 | 0.075 | 0.460 | 97 | 0.105 | 0.419 | 81 |
| | DL2 | 0.132 | 0.504 | 113 | 0.160 | 0.460 | 74 | 0.158 | 0.419 | 27 |
| | DL3 | 0.199 | 0.291 | 12 | 0.216 | 0.311 | 10 | 0.209 | 0.334 | 16 |
| | DL4 | 0.232 | 0.291 | 50 | 0.220 | 0.311 | 58 | 0.226 | 0.334 | 54 |
| | DL5 | 0.386 | 0.291 | 90 | 0.387 | 0.311 | 88 | 0.363 | 0.334 | 101 |
| CB SFSI | DL1 | 0.068 | 0.463 | 96 | 0.090 | 0.506 | 150 | 0.132 | 0.387 | 124 |
| | DL2 | 0.165 | 0.463 | 97 | 0.210 | 0.506 | 44 | 0.205 | 0.387 | 24 |
| | DL3 | 0.226 | 0.303 | 40 | 0.258 | 0.329 | 7 | 0.254 | 0.281 | 40 |
| | DL4 | 0.321 | 0.303 | 61 | 0.284 | 0.329 | 89 | 0.350 | 0.281 | 59 |
| | DL5 | 0.440 | 0.303 | 39 | 0.455 | 0.329 | 39 | 0.518 | 0.281 | 23 |
| CB FSFI | DL1 | 0.069 | 0.446 | 98 | 0.092 | 0.443 | 130 | 0.142 | 0.352 | 121 |
| | DL2 | 0.170 | 0.446 | 99 | 0.214 | 0.443 | 60 | 0.250 | 0.352 | 20 |
| | DL3 | 0.229 | 0.292 | 40 | 0.219 | 0.322 | 3 | 0.286 | 0.277 | 42 |
| | DL4 | 0.333 | 0.292 | 65 | 0.295 | 0.322 | 90 | 0.359 | 0.277 | 55 |
| | DL5 | 0.469 | 0.292 | 30 | 0.470 | 0.322 | 33 | 0.517 | 0.277 | 22 |

**Table 7** Annex: Value of fragility curves for A2 and soil S3

| | | SU1 | | | SU2 | | | SU4 | | |
|---|---|---|---|---|---|---|---|---|---|---|
| | | $IM_{50}$ [g] | σ | N analyses | $IM_{50}$ [g] | σ | N analyses | $IM_{50}$ [g] | σ | N analyses |
| FB C | DL1 | 0.043 | 0.375 | 36 | 0.055 | 0.421 | 63 | 0.075 | 0.380 | 57 |
| | DL2 | 0.104 | 0.375 | 102 | 0.124 | 0.421 | 85 | 0.123 | 0.380 | 21 |
| | DL3 | 0.184 | 0.350 | 15 | 0.225 | 0.372 | 9 | 0.139 | 0.356 | 35 |
| | DL4 | 0.207 | 0.350 | 37 | 0.190 | 0.372 | 38 | 0.189 | 0.356 | 47 |
| | DL5 | 0.321 | 0.350 | 141 | 0.323 | 0.372 | 137 | 0.319 | 0.356 | 144 |

**Table 7** Annex: Value of fragility curves for A2 and soil S3

| | | SU1 | | | SU2 | | | SU4 | | |
|---|---|---|---|---|---|---|---|---|---|---|
| | | $IM_{50}$ [g] | σ | N analyses | $IM_{50}$ [g] | σ | N analyses | $IM_{50}$ [g] | σ | N analyses |
| CB SFSI | DL1 | 0.057 | 0.436 | 73 | 0.086 | 0.389 | 105 | 0.126 | 0.396 | 135 |
| | DL2 | 0.153 | 0.436 | 132 | 0.191 | 0.389 | 89 | 0.228 | 0.396 | 37 |
| | DL3 | 0.266 | 0.327 | 54 | 0.209 | 0.351 | 3 | 0.295 | 0.341 | 52 |
| | DL4 | 0.371 | 0.327 | 49 | 0.328 | 0.351 | 96 | 0.388 | 0.341 | 56 |
| | DL5 | 0.432 | 0.327 | 26 | 0.439 | 0.351 | 21 | 0.460 | 0.341 | 8 |
| CB FSFI | DL1 | 0.059 | 0.420 | 76 | 0.084 | 0.389 | 97 | 0.127 | 0.369 | 121 |
| | DL2 | 0.158 | 0.420 | 131 | 0.187 | 0.389 | 98 | 0.232 | 0.369 | 45 |
| | DL3 | 0.266 | 0.329 | 52 | 0.244 | 0.350 | 6 | 0.299 | 0.334 | 47 |
| | DL4 | 0.379 | 0.329 | 50 | 0.336 | 0.350 | 90 | 0.384 | 0.334 | 54 |
| | DL5 | 0.428 | 0.329 | 24 | 0.434 | 0.350 | 21 | 0.460 | 0.334 | 11 |

**Table 8** Annex: Value of fragility curves for A2 and soil S4

| | | SU1 | | | SU2 | | | SU4 | | |
|---|---|---|---|---|---|---|---|---|---|---|
| | | $IM_{50}$ [g] | σ | N analyses | $IM_{50}$ [g] | σ | N analyses | $IM_{50}$ [g] | σ | N analyses |
| FB C | DL1 | 0.113 | 0.412 | 119 | 0.126 | 0.449 | 151 | 0.188 | 0.342 | 59 |
| | DL2 | 0.217 | 0.412 | 71 | 0.243 | 0.449 | 53 | | | 0 |
| | DL3 | 0.309 | 0.265 | 19 | | | 0 | 0.262 | 0.276 | 22 |
| | DL4 | 0.290 | 0.265 | 9 | 0.296 | 0.271 | 15 | 0.267 | 0.276 | 25 |
| | DL5 | 0.412 | 0.265 | 70 | 0.413 | 0.271 | 70 | 0.413 | 0.276 | 73 |
| CB SFSI | DL1 | 0.114 | 0.407 | 92 | 0.155 | 0.476 | 187 | 0.236 | 0.398 | 141 |
| | DL2 | 0.253 | 0.407 | 126 | 0.333 | 0.476 | 44 | 0.387 | 0.398 | 13 |
| | DL3 | 0.373 | 0.264 | 29 | | | 0 | 0.438 | 0.234 | 18 |
| | DL4 | 0.473 | 0.264 | 12 | 0.449 | 0.269 | 33 | 0.493 | 0.234 | 15 |
| | DL5 | 0.522 | 0.264 | 9 | 0.511 | 0.269 | 7 | | | 0 |
| CB FSFI | DL1 | 0.120 | 0.407 | 93 | 0.158 | 0.475 | 181 | 0.244 | 0.377 | 130 |
| | DL2 | 0.261 | 0.407 | 127 | 0.341 | 0.475 | 48 | 0.415 | 0.377 | 18 |
| | DL3 | 0.420 | 0.237 | 25 | 0.441 | 0.238 | 5 | 0.451 | 0.243 | 16 |
| | DL4 | 0.483 | 0.237 | 15 | 0.457 | 0.238 | 31 | 0.487 | 0.243 | 11 |
| | DL5 | | | 0 | | | 0 | 0.587 | 0.243 | 5 |

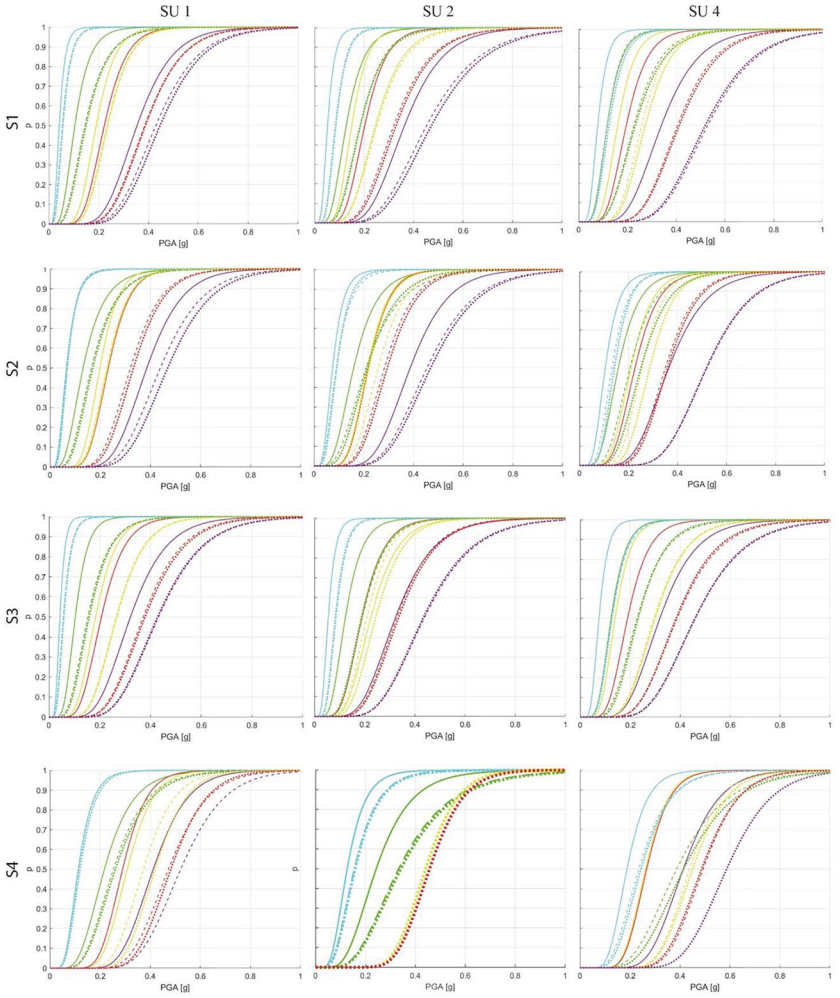


**Fig. 2** Annex: Fragility curves for A2

**Acknowledgements** The study presented in this article was developed in the framework of the MARS project (WP4), carried out within the activities of the ReLUIS-DPC 2022–2024 research program, funded by the Presidenza del Consiglio dei Ministri-Dipartimento della Protezione Civile (DPC) and WP16 (Task 16.2, Soil-Foundation-Structure Interaction) within the activities of the ReLUIS-DPC 2024–2026 research program. Note that the opinions and conclusions presented by the authors do not necessarily reflect those of the funding entity.

**Author contributions** Enza Zeolla: investigation; data curation on geotechnical aspects; writing-original draft. Andrea Brunelli: investigation; data curation; carrying out numerical analyses; writing-original draft. Filomena de Silva: conceptualization; supervision; methodology; review & editing. Serena Cattari: conceptualization; supervision; software; methodology; writing-review & editing. Stefania Sica: conceptualization; supervision; methodology; writing-review & editing.

**Funding** Open access funding provided by Università degli Studi di Genova within the CRUI-CARE Agreement.

## Declarations

**Ethical approval** The authors declare that they recognize the principles of the journal and have adopted a conflict-of-interest policy compliant with international, national and institutional standards on research involving human and animal participants and on informed consent. The research did not involve the use of animals in any part of it.

**Competing interests** The authors have no relevant financial or non-financial interests to disclose.



## References

Ademović N, Toholj M, Radonić D, Casarin F, Komesar S, Ugarković K (2022) Post-earthquake assessment and strengthening of a cultural-heritage residential masonry building after the 2020 Zagreb earthquake. Buildings 12(11):2024. https://doi.org/10.3390/buildings12112024

Ambrosino A, Sica S (2024) The role of underground archaeological remains on the seismic response of a historic tower. Soil Dyn Earthq Eng 187:109017

Ambrosino A, De Angelis A, Pecce MR, Sica S (2023) Effect of soil-structure interaction on the dynamic identification of a prestressed concrete bridge. In Proceedings of COMPDYN 2023 (Vol. 2, pp. 4144–4155)

Angiolilli M, Brunelli A, Cattari S (2023) Fragility curves of masonry buildings in aggregate accounting for local mechanisms and site effects. Bull Earthq Eng 21:2877–2919

Azadi MRE, Soltani AA (2010) The effects of soil-foundation-structure interaction on the dynamic response of Delijan cement-storage silo under earthquake loading. Electron J Geotech Eng 15:659–676

Battaglia L, Ferreira TM, Lourenço PB (2021) Seismic fragility assessment of masonry Building aggregates: A case study in the old City centre of Seixal, Portugal. Earthq Eng Struct Dyn 50(5):1358–1377

Betti R (1997) Effects of the dynamic cross-interaction in the seismic analysis of multiple embedded foundations. Earthq Eng Struct Dyn 26(10):1005–1019

Bianchini N, Ciocci MP, Solarino F et al (2023) Influence of wall-to-floor connections and pounding on pre- and post-diction simulations of a masonry Building aggregate tested on a shaking table. Bull Earthq Eng. https://doi.org/10.1007/S10518-023-01641-X

Bordón JDR, Aznárez JJ, Padrón LA, Maeso O, Bhattacharya S (2019) Closed-form stiffnesses of multi-bucket foundations for OWT including group effect correction factors. Mar Struct 65:326–342

Brunelli A, de Silva F, Cattari S (2021a) On the site-amplification and soil-structure interaction in URM structures: Use of fragility curves to assess the simplified code-approach. In: 8th COMPDYN Proceedings, Athens, Greece, 28–30 June 2021

Brunelli A, de Silva F, Piro A et al (2021b) Numerical simulation of the seismic response and soil–structure interaction for a monitored masonry school Building damaged by the 2016 central Italy earthquake. Bull Earthq Eng 19. https://doi.org/10.1007/s10518-020-00980-3

Brunelli A, de Silva F, Cattari S (2022a) Site effects and soil-foundation-structure interaction: derivation of fragility curves and comparison with Codes-conforming approaches for a masonry school. Soil Dyn Earthq Eng 154:107125

Brunelli A, de Silva F, Cattari S (2022b) Observed and simulated urban-scale seismic damage of masonry buildings in aggregate on soft soil: the case of visso hit by the 2016/2017 central Italy earthquake. Int J Disaster Risk Reduct 83:103391

Brunelli A, Alleanza GA, Cattari S, De Silva F, d'Onofrio A (2022c) In: Lancellotta R, Viggiani C et al (eds) Simulation of damage observed on buildings in aggregate after the 2016–2017 central Italy earthquake accounting for site effects and Soil-Structure interaction. TC 301 geotechnical engineering for the preservation of monuments and historic sites, naple, Italy. Geotechnical Engineering for the Preservation of Monuments and Historic Sites III

Bybordiani M, Arici Y (2019) Structure–soil–structure interaction of adjacent buildings subjected to seismic loading. Earthq Eng Struct Dyn 48(7):731–748
Carocci CF (2012) Small centres damaged by 2009 L'Aquila earthquake: on site analyses of historical masonry aggregates. Bull Earthq Eng 10:45–71
Cattari S, Angiolilli M (2022) Multiscale procedure to assign structural damage levels in masonry buildings from observed or numerically simulated seismic performance. Bull Earthq Eng 20:7561–7607
Cattari S, Lagomarsino S (2013) Masonry structures. In: Sullivan T, Calvi G (eds) Developments in the field of displacement based seismic assessment. IUSS Press and EUCENTRE, Pavia, pp 151–200
Cattari S, Camilletti D, Lagomarsino S et al (2018a) Masonry Italian Code-Conforming buildings. Part 2: nonlinear modelling and Time-History analysis. J Earthquake Eng 22:2010–2040
Cattari S, Degli Abbati S, Ottonelli D et al (2018b) ReLUIS-Task 4.1 workgroup report, report Di sintesi sulle attività Svolte Sugli edifici in muratura monitorati Dall'Osservatorio Sismico Delle strutture. Linea Strutture in Muratura
Cattari S, Alfano S, Ottonelli D, Saler E, da Porto F (2021) Comparative study on two analytical mechanical-based methods for deriving fragility curves targeted to masonry school buildings. *8th ECCOMAS COMPDYN Conference*. Athens, Greece, 27–30 June 2021
Cattari S, Alfano S, Manfredi V, Borzi B, Faravelli M et al (2024) National Risk Assessment of Italian School Buildings: The Mars Project Experience. Available at SSRN: https://ssrn.com/abstract=4788831 or https://doi.org/10.2139/ssrn.4788831
CEN (2004) EN 1998-1, Eurocode 8: Design of structures for earthquake resistance - Part 1: General rules, seismic actions and rules for buildings. Brussels: CEN, 2004
Chieffo N, Formisano A (2019) Comparative seismic assessment methods for masonry Building aggregates: A case study. Front Built Environ, 5
Chiumiento G, Formisano A (2019) Simplified and refined analyses for seismic investigation of historical masonry clusters: comparison of results and influence of the structural units position. Front Built Environ 5:1–13
Ciancimino A, Lanzo G, Alleanza GA et al (2020) Dynamic characterization of fine-grained soils in central Italy by laboratory testing. Bull Earthq Eng 18:5503–5531
d'Onofrio A, Silvestri F (2001) Influence of Micro-Structure on Small-Strain Stiffness and Damping of Fine Grained Soil and Effects on Local Site Response. In: International Conferences on Recent Advances in Geotechnical Earthquake Engineering and Soil Dynamics
De Angelis A, Ambrosino A, Sica S, Lourenco PB (2022a) Soil contribution on the structural identification of a historical masonry bell-tower: simplified vs advanced numerical models. Geotechnical engineering for the preservation of monuments and historic sites III. CRC, pp 904–916
De Angelis A, Lourenço PB, Sica S, Pecce MR (2022b) Influence of the ground on the structural identification of a bell-tower by ambient vibration testing. Soil Dyn Earthq Eng 155:107102
de Silva F, Ceroni F, Sica S, Silvestri F (2018) Non-linear analysis of the Carmine bell tower under seismic actions accounting for soil–foundation–structure interaction. Bull Earthq Eng 16(7):2775–2808
de Silva F, Silvestri F (2025) Derivation, validation, and web application of dimensionless analytical solutions for equivalent period and damping ratio of soil-foundation-structure systems. J Geotech Geoenviron Eng 151(6):04025049. https://doi.org/10.1061/JGGEFK.GTENG-12927
Demsic M, Pinasco S, Pilipovic A, Cattari S, Lagomarsino S, Savor Novak M, Uros M (2024) Development of fragility curves of masonry buildings build in a regular row aggregate. 18th WCEE, 30 June-5 July 2024, Milan, Italy
Fathi A, Sadeghi A, Emami Azadi MR, Hoveidae N (2020) Assessing the soil-structure interaction effects by direct method on the out-of-plane behavior of masonry structures (case study: Arge-Tabriz). Bull Earthq Eng 18:6429–6443
Formisano A (2017) Theoretical and numerical seismic analysis of masonry Building aggregates: case studies in San Pio Delle Camere (L'Aquila, Italy). J Earthquake Eng 21(2):227–245
Formisano A, Chieffo N, Clementi F, Mosoarca M (2021) Influence of local site effects on the typological fragility curves for Class-Oriented masonry buildings in aggregate condition. Open Civ Eng J, 5
Garini E, Anastasopoulos I, Gazetas G (2020) Soil, basin and soil–building–soil interaction effects on motions of Mexico City during seven earthquakes. Géotechnique 70(7):581–607
Gazetas G (1991) Formulas and charts for impedances of surface and embedded foundations. J Geotech Eng 117:1363–1381
Grünthal G (1998) European Macroseismic Scale 1998 (EMS-98). Luxembourg
Güllü H, Jaf HS (2016) Full 3D nonlinear time history analysis of dynamic soil–structure interaction for a historical masonry arch Bridge. Environ Earth Sci 75:1–17
Hardin BO, Kalinski ME (2005) Estimating the shear Modulus of gravelly soils. J Geotech GeoEnviron Eng 131:867–875

Kottke AR, Rathje EM (2008) Technical manual for strata. Report no. 2008/10. Pacific Earthquake Engineering Research Center, University of California
Lagomarsino S, Cattari S (2014) Fragility Function of Masonry Buildings. SYNER-G: Typology Definition and Fragility Functions for Physical Elements at Seismic Risk: Buildings, Lifelines, Transportation Networks and Critical Facilities, Pitilakis K, Crowley H, Kaynia AM eds., 2014
Lagomarsino S, Giovinazzi S (2006) Macroseismic and mechanical models for the vulnerability assessment of current buildings. Bull Earthq Eng 4(4):415–443
Lagomarsino S, Masi A (2021) Report finale: mappe di rischio sismico dell'edilizia residenziale, Report del progetto DPC-ReLUIS 2019–2021 WP4-Mappe di rischio e scenari di danno sismico (MARS), In Italian, available from ww.reluis.it
Lagomarsino S, Penna A, Galasco A, Cattari S (2013) TREMURI program: an equivalent frame model for the nonlinear seismic analysis of masonry buildings. Eng Struct 56:1787–1799
Liao T, Massoudi N, Mchood M et al (2013) Normalized shear modulus of compacted gravel. In: 18th international conference on soil mech Geotech eng. (ICSMGE). Paris
Malomo D, Dejong MJ (2022) M-DEM simulation of seismic pounding between adjacent masonry structures. Bull Earthq Eng, 0123456789
Maravas A, Mylonakis G, Karabalis DL (2014) Simplified discrete systems for dynamic analysis of structures on footings and piles. Soil Dyn Earthq Eng 61–62:29–39
Masi A, Lagomarsino S, Dolce M et al (2021) Towards the updated Italian seismic risk assessment: exposure and vulnerability modelling. Bull Earthq Eng 19:3253–3286
Masi A, Lagomarsino S, Manfredi V, Nicodemo G (2022) The Italian seismic risk maps: an overview of the methodology and results of MARS project. *3rd Euopean Conference on Earthquake Engineering & Seismology, Bucharest, Romania*, 2022
Masing G (1926) Eigenspannungen und Verfestigung beim messing. In: 2nd Int congress of App Mech. Zurich
Mulliken JS, Karabalis DL (1998) Discrete model for dynamic through-the-soil coupling of 3-D foundations and structures. Earthq Eng Struct Dynamics 27(7):687–710
Mylonakis G, Nikolaou S, Gazetas G (2006) Footings under seismic loading: analysis and design issues with emphasis on Bridge foundations. Soil Dyn Earthq Eng 26(9):824–853
MZS3 (2018) Report of the 3rd level Seismic Microzonation of Visso village. Approved by the Working Group. https://www.comune.visso.mc.it/avvisi-cms/microzonazione-sismica-iii-livello/
NIST (2012) Soil-structure interaction for Building structures. Report no. GCR 12-917-21, prepared by the NEHRP consultants joint venture (a partnership of the applied technology Council and consortium of universities for research in earthquake Engineering). for the National Institute of Standards and Technology, Washington D.C.
NTC (2018) Norme Tecniche per le Costruzioni. DM 17/1/2018, Italian Ministry of Infrastructure and Transportation, G.U. n. 42, 20 February 2018, Rome, Italy, 2018 (in Italian)
Outayeb S, Louadj S, Louzai A (2023) Soil-class effects on the seismic response of RC moment-resisting frames considering soil-structure interaction. Asian J Civil Eng 24(8):2739–2754
Padron LA, Aznarez JJ, Maeso O (2009) Dynamic structure–soil–structure interaction between nearby piled buildings under seismic excitation by BEM–FEM model. Soil Dyn Earthq Eng 29(6):1084–1096
Padrón LA, Aznárez JJ, Maeso O (2008) Dynamic analysis of piled foundations in stratified soils by a BEM–FEM model. Soil Dyn Earthq Eng 28(5):333–346
Pagnini LC, Vicente RS, Lagomarsino S, Varum H (2011) A mechanical model for the seismic vulnerability assessment of old masonry buildings. Earthq Struct 2(1):25–42
Pais A, Kausel E (1988) Approximate formulas for dynamic stiffnesses of rigid foundations. Soil Dyn Earthq Eng 7(4):213–227
Pinasco S, Lagomarsino S, Cattari S (2024) Unreinforced masonry buildings in aggregate of urban settlements: current approaches and critical issues for the seismic vulnerability assessment, submitted to structures, Elsevier, *first round of review received*
Piro A, de Silva F, Parisi F, di Scotto A, Silvestri F (2020) Effects of soil-foundation-structure interaction on fundamental frequency and radiation damping ratio of historical masonry Building sub-structures. Bull Earthq Eng 18:1187–1212
Ponte M, Guerrini G, Penna A, Bento R (2024) Modelling of interactions between adjacent historical buildings built in different phases. 18th WCEE, 30 June-5 July 2024, Milan, Italy
Qian J, Beskos DE (1995) Dynamic interaction between 3-D rigid surface foundations and comparison with the ATC-3 provisions. Earthq Eng Struct Dynamics 24(3):419–437
Qian J, Beskos DE (1996) Harmonic wave response of two 3-D rigid surface foundations. Soil Dyn Earthq Eng 15(2):95–110
Ramberg W, Osgood W (1943) Description of stress-strain curves by three parameters. In: Natl Advis Comm Aeronaut. Washington DC

Régnier J, Bonilla LF, Bard PY, Bertrand E, Hollender F, Kawase H, Sicilia D, Arduino P, Amorosi A, Asimaki D, Boldini D, Chen L, Chiaradonna A, DeMartin F, Elgamal A, Falcone G, Foerster E, Foti S, Garini E, Gazetas G, Gélis C, Ghofrani A, Giannakou A, Gingery J, Glinsky N, Harmon J, Hashash Y, Iai S, Kramer S, Kontoe S, Kristek J, Lanzo G, di Lernia A, Lopez-Caballero F, Marot M, McAllister G, Diego Mercerat E, Moczo P, Montoya-Noguera S, Musgrove M, Nieto-Ferro A, Pagliaroli A, Passeri F, Richterova A, Sajana S, Santisi d'Avila MP, Shi J, Silvestri F, Taiebat M, Tropeano G, Vandeputte D, Verrucci L (2018) PRENOLIN: International benchmark on 1D nonlinear site-response analysis—Validation phase exercise. Bull Seismol Soc Am 108(2):876–900

Rossetto T, D'Ayala D, Ioannou I, Meslem A (2014) Evaluation of Existing Fragility Curves. In: Pitilakis K, Crowley H, Kaynia A. (eds) SYNER-G: Typology Definition and Fragility Functions for Physical Elements at Seismic Risk. Geotechnical, Geological and Earthquake Engineering, 27. https://doi.org/10.1007/978-94-007-7872-6_3

Salvatori C, Guerrini G, Graziotti F, Penna A (2024) Effect of the interaction among adjacent structural units in aggregates subjected to seismic actions. 18th WCEE, 30 June-5 July 2024, Milan, Italy

Sextos A, De Risi R, Pagliaroli A, Foti S, Passeri F, Ausilio E, Zimmaro P (2018) Local site effects and incremental damage of buildings during the 2016 central Italy earthquake sequence. Earthq Spectra 34(4):1639–1669

Smerzini C, Paolucci R (2013) SIMBAD: a database with Selected Input Motions for displacement Based Assessment and Design – 3rd release by Department of Structural Engi-neering, Research Project DPC RELUIS. Milano, Italy

Smerzini C, Galasso C, Iervolino I, Paolucci R (2014) Ground motion record selection based on broadband spectral compatibility. Earthq Spectra 30:1427–1448

Tsogka C, Wirgin A (2003) Simulation of seismic response in an idealized City. Soil Dyn Earthq Eng 23(5):391–402

Turnsek V, Cacovic F (1971) Some experimental results on the Strength of Brick Masonry Walls. Proc. 2nd Int. Brick Mason. Conf., Stoke-on-Trent, United Kingdom

Ulrich T, Negulescu C, Ducellier A (2015) Using the discrete element method to assess the seismic vulnerability of aggregated masonry buildings. Bull Earthq Eng 13(10):3135–3150

Valluzzi MR, Sbrogiò L, Saretta Y, Wenliuhan H (2022) Seismic response of masonry buildings in historical centres struck by the 2016 central Italy earthquake. Impact of Building features on damage evaluation. Int J Architectural Herit 16(12):1859–1884

Villar S, Di Trapani F, Di Benedetto M, Petracca M, Camata G (2024) Refined modelling and analysis of building aggregates for the assessment of seismic response. 18th WCEE, 30 June-5 July 2024, Milan, Italy

Warburton GB, Richardson JD, Webster JJ (1971) Forced vibrations of two masses on an elastic half space

Zeolla E, de Silva F, Sica S (2023) A simplified approach to account for through-soil interaction between two adjacent shallow foundations. Bull Earthq Eng 21(5):2503–2532

Zeolla E, de Silva F, Sica S (2024) Towards a practice-oriented procedure to account for static and dynamic interaction among three adjacent shallow foundations. Comput Geotech 170:106242

Zhang Z, Davis L, Malomo D (2024) Simplified assessment of the in-plane seismic response of old brick masonry building aggregates using DE macro-crack networks. Structural Analysis of Historical Constructions. SAHC 2023. RILEM Bookseries, 46:217–231. Springer

## Authors and Affiliations

**E. Zeolla[1] · A. Brunelli[2] · F. de Silva[3] · S. Cattari[2] · S. Sica[1]**

✉ A. Brunelli
andrea.brunelli@edu.unige.it

E. Zeolla
ezeolla@unisannio.it

F. de Silva
filomena.desilva@unina.it

S. Cattari
serena.cattari@unige.it

S. Sica
stefsica@unisannio.it

[1] University of Sannio, Benevento, Italy

[2] University of Genoa, Genoa, Italy

[3] University of Federico II, Naples, Italy